1
Applications of Electrochemistry in the Fabrication and Characterization of Thin-Film Solar Cells

Phillip Dale and Laurence Peter

1.1
Introduction

Tackling climate change has become a priority for the scientific as well as the political community. The European Union has set a target for photovoltaic (PV)-generated electricity to become competitive with conventional electricity generation by 2020–2030, and the Council of the European Union aims to reduce greenhouse gas emission by 60–80% by 2050. The UK's Stern Review [1], which deals with the economic impact of global climate change, states that "the benefits of strong, early action on climate change outweigh the costs" and goes on to identify "development of a range of low-carbon and high-efficiency technologies on an urgent timescale" as essential to any strategy that aims to address the problems of climate change. These targets have implications for the science and technology of PV. If PV is to make a major contribution to a low-carbon energy economy, issues of materials and manufacturing costs [2] as well as materials sustainability need to be considered. Current non-silicon PV technologies are based on cadmium telluride and the chalcopyrite materials $Cu(In,Ga)Se_2$ (CIGS) and $CuInS_2$. Both of these materials are unlikely to be sustainable in the long term for terawatt deployment [3] of terrestrial PV, so that a search for alternative materials has assumed considerable importance.

Figure 1.1 illustrates the nature of the problem by summarizing the natural abundance and raw elemental costs for materials that are used in thin-film solar cells. It is important to note that a logarithmic scale has been used for both the abundance and the raw materials cost. The most expensive material by far is indium, and the availability and cost of indium have become geopolitical issues in recent months since it is used in the manufacture of liquid crystal displays and touch screens.

The rarest element shown in Figure 1.1 is tellurium, and it is reasonable to suppose that this has implications for the long-term sustainability of cadmium telluride solar cell technology. Sustainability issues of this kind provide the rationale for expansion of the range materials that deserve study for PV applications. A promising new candidate for sustainable PV is Cu_2ZnSnS_4

Advances in Electrochemical Science and Engineering. Edited by Richard C. Alkire, Dieter M. Kolb, Jacek Lipkowski, and Philip N. Ross

ISBN: 978-3-527-32859-8

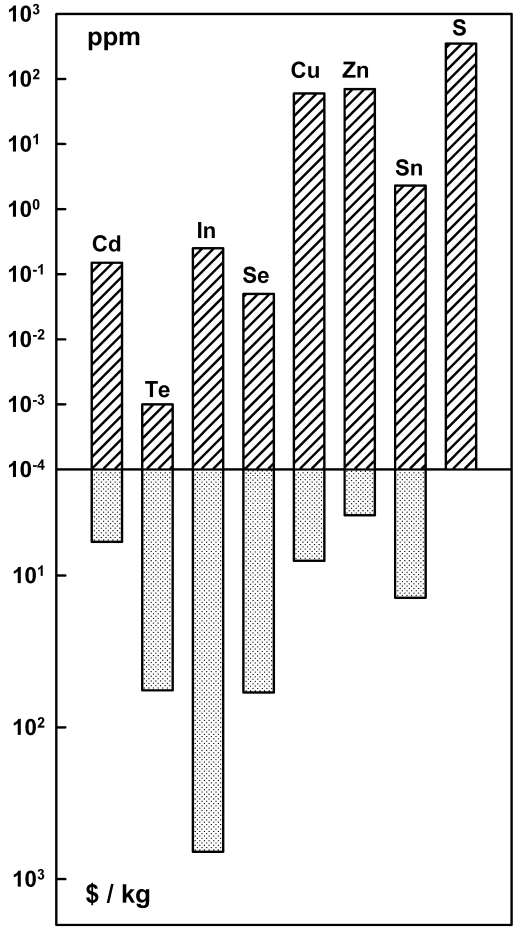

Figure 1.1 Comparison of availability and costs of elements used for the fabrication of solar cells. Note the logarithmic scales.

(CZTS), a compound with electronic properties similar to those of CIGS that contains cheap and plentiful non-toxic elements. However, remarkably little work has been carried out to characterize the potential of this material for PV applications.

Sustainability and environmental issues are also associated with the fabrication processes used in PV. The authors of this chapter believe that electrochemical methods have the potential for large-scale low-cost preparation of PV materials [4], and, in addition, electrochemical methods are powerful tools for the characterization of PV materials and device components [5]. These two topics are explored in the present chapter.

1.2
Electrochemical Routes to Thin-Film Solar Cells

1.2.1
Basic Cell Configurations

Examples of thin-film PV devices based on compound semiconductor absorber films are shown in Figure 1.2. The n-CdS|p-CdTe solar cell (Figure 1.2a) is an example of a superstrate cell. The thin CdS layer is grown on glass coated with a transparent conducting layer (e.g., fluorine-doped tin oxide, FTO). CdTe is then deposited onto the CdS layer and, following thermal treatment, the device is completed by the addition of ohmic contacts to the CdTe. CIGS solar cells are mostly made in the substrate configuration (Figure 1.2b) where the CIGS is deposited onto a metallic back contact, for example Mo-coated glass (although efficient CIGS superstrate cells have also been fabricated). The CIGS is coated with a thin CdS layer followed by a layer of intrinsic ZnO and a layer of Al-doped ZnO, which acts as a conducting transparent top contact. An Al grid is used to collect the current.

CdTe devices have achieved 16.7% efficiency in the laboratory [6], whereas CIGS cells have reached 20.0% [7]. The most efficient CIGS devices contain around 30% Ga distributed non-uniformly through the film, with higher concentrations preferred at the front and back of the layer. Kesterites are emerging as suitable In-free materials for absorber layers, but current understanding of the factors that

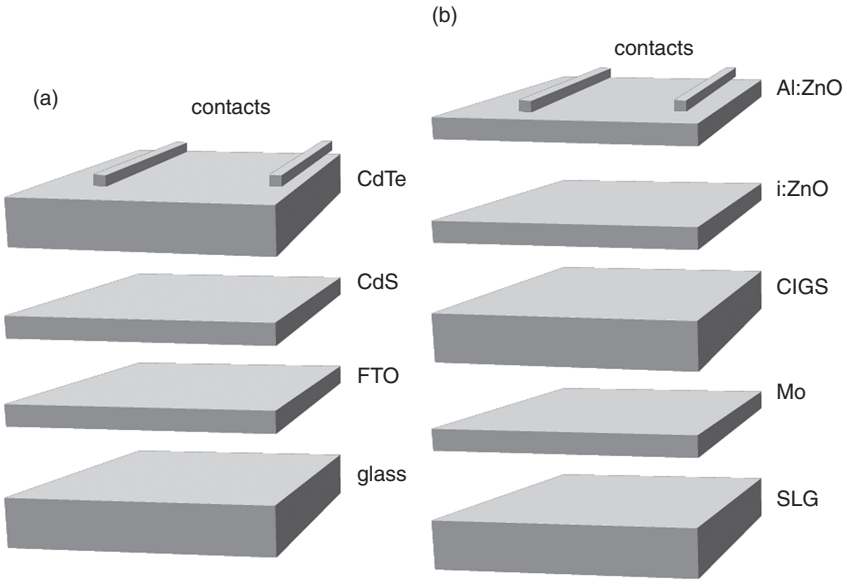

Figure 1.2 Comparison of superstrate and substrate solar cell configurations. (a) Superstrate configuration used for CdS|CdTe solar cells. (b) Substrate configuration commonly used for CIGS solar cells.

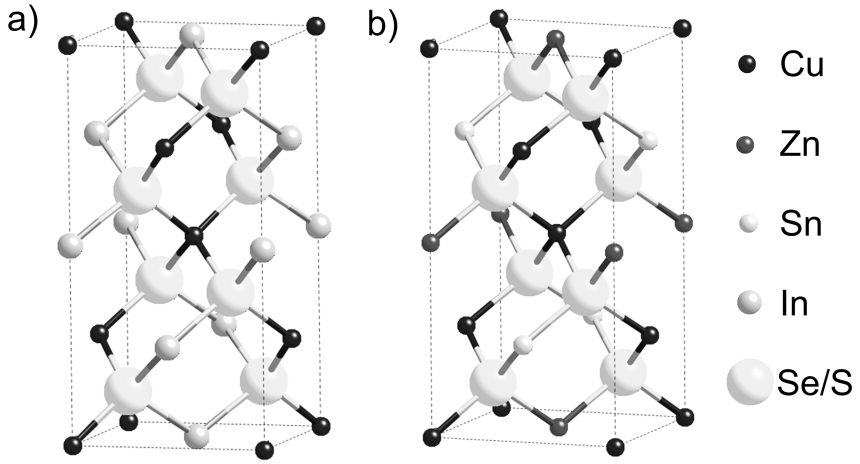

Figure 1.3 Crystal structures of (a) chalcopyrite and (b) kesterite [12].

determine the optoelectronic properties of these materials is limited. The best kesterite-based devices, like CIGS devices, have absorber layers that are Cu deficient [8, 9]. The best published efficiency of 6.7% has been reported by Katagiri *et al.* [10] for a device that is Zn rich and Sn deficient. Our research has shown that CZTS device performance improves if the surface of the absorber layer is etched in KCN which is known to remove CuS phases [11].

The kesterite structure Cu_2ZnSnS_4 is isoelectronic with chalcopyrite $CuInS_2$. Half of the In(III) atoms are replaced with Zn(II) atoms, and the other half are replaced with Sn(IV) atoms. The crystal structures of the chalcopyrite and kesterite are shown in Figure 1.3.

The methods available for preparation of the different layers in thin-film solar cells include physical methods such as vacuum sputtering, vapor-phase deposition, and molecular beam epitaxy as well as chemical methods such as chemical vapor-phase deposition, metal organic vapor-phase epitaxy, chemical bath deposition (CBD), and electrochemical deposition (ED). This chapter explores the potential of electrodeposition as a route to the fabrication of absorber layers such as CdTe, CIGS, and CZTS for thin-film solar cells. Electrochemistry may also be useful for the preparation of transparent layers such as ZnO; this topic has been reviewed by Pauporte and Lincot [13].

1.2.2
Material Requirements for PV Applications

In this section we discuss first the general materials requirements for an absorber layer. Specific issues for particular materials are then considered in subsequent sections. The specific optoelectronic properties of each absorber layer will not be

discussed in detail here, but rather the structural, chemical, and morphological properties of the layer that are required to minimize electrical losses. For specifics, the interested reader is referred to reviews of each material: CdTe [14, 15], $Cu(In,Ga)(S,Se)_2$ [8, 15], and kesterite [16]. For the fundamentals of semiconductor physics, the reader is referred to standard textbooks, for example Sze [17].

The electron–hole pairs that are created in the absorber layer when light is absorbed are driven to the contacts by the Fermi level gradients in the device [18]. Loss of these carriers is due either to recombination or to electrical shorting. In order to minimize recombination, the absorber layer should be crystalline with as few lateral grain boundaries and chemical impurities as possible. The material should be single phase without parasitic secondary phases, which in the worst case act as recombination centers and in the best case just reduce the photogeneration volume. If secondary phases extend through the absorber layer, they may give rise to electrical shorting. Similarly, if there are pinholes between the individual grains of the film, subsequent deposition of the next layer may lead to shorting.

For use in PV devices, the absorber layer must be uniform laterally on both the micrometer and centimeter length scales with respect to its composition, and vertically on the micrometer length scale with respect to its thickness. Lateral uniformity on the centimeter scale is a prerequisite for fabrication of larger area PV devices, and the vertical thickness needs to be uniform in order to avoid stress in subsequent deposited layers and to avoid pinhole formation. A final criterion to consider is that the absorber layer must adhere well to the substrate so that it can withstand subsequent thermal treatment.

1.2.2.1 Implications of Materials Requirements for the Direct Synthesis of Absorber Layers by Electrodeposition

Compound semiconductor absorber layers for PV applications are complex multi-element materials with stringent requirements regarding structure, composition, and morphology. Meeting these requirements presents formidable challenges for any electrodeposition process. Even in those cases where the desired material can be obtained directly by electrodeposition, additional treatments are required before electrodeposited layers can be used in working PV devices. In other cases, a two-step electrodeposition and annealing process is required to obtain PV-grade material. For work prior to 1995, the reader is referred to Pandey [19].

The absorber layer in the thin-film solar cells considered here is typically a polycrystalline p-type compound semiconductor with grain sizes of the order of a micrometer. In order to electrodeposit such a thin film directly, a number of criteria have to be fulfilled. The nucleation density must not be too high so that large grains can be grown uniformly, and secondary nucleation should be avoided if possible. At the same time, overlap of the grains should not leave pinholes that lower the shunt resistance of the device. The layer should also be reasonably flat to minimize recombination losses, and its composition should be as ideal as possible, with low impurity concentrations.

The requirement for strict control of stoichiometry has three consequences. Firstly, electrons need to be readily available for the reduction of ionic precursor

species. This can be a problem if the deposit is p-type. Secondly, deposited atoms must be incorporated into the correct positions in the growing semiconductor lattice. However, these may not be the lowest energy positions on the surface, and if atoms are deposited elsewhere, there may be insufficient thermal energy to move them to minimum energy positions. Thirdly, the deposition rates of the atomic constituents have to be controlled so that the correct atoms are deposited in the correct order. While it may be possible to satisfy some of the requirements regarding morphology and stoichiometry in an ED process, it is virtually impossible to satisfy all of them at the same time. Possibly the closet approach to ideal deposition has been achieved in electrochemical atomic layer epitaxy (ECALE) [20–22]. This method involves layer-by-layer growth, where a solution of single component is flowed over the substrate and one monolayer is deposited and then the solution is removed and replaced by another with the next species to be deposited. This process is repeated many times to form the semiconductor of interest. This approach works particularly well on single-crystal substrates [21], but it is not suitable for a large-area commercial fabrication process.

ED often produces compact pinhole-free compound semiconductor films with the correct global stoichiometry, but with small grain sizes of between 50 and 100 nm. Figures 1.4a and 1.4b compare an as-deposited $CuInSe_2$ precursor film with an annealed film. The crystalline quality of the films can be improved by annealing them at high temperature. The optoelectronic properties also improve, and the films have been used to fabricate devices of 6.7% efficiency [23], in spite of the fact that only small grain growth is observed in the SEM image of Figure 1.4b.

The XRD pattern for the as-deposited film depicted in Figure 1.5a shows the main characteristic reflexes of the chalcopyrite phase, but the peaks are broad, indicating poor crystallinity. The optoelectronic properties of the as-deposited films are also poor (see Section 1.3). A narrowing of the reflexes in the XRD pattern is observed after annealing the film (Figure 1.5b), confirming the improvement in crystallinity.

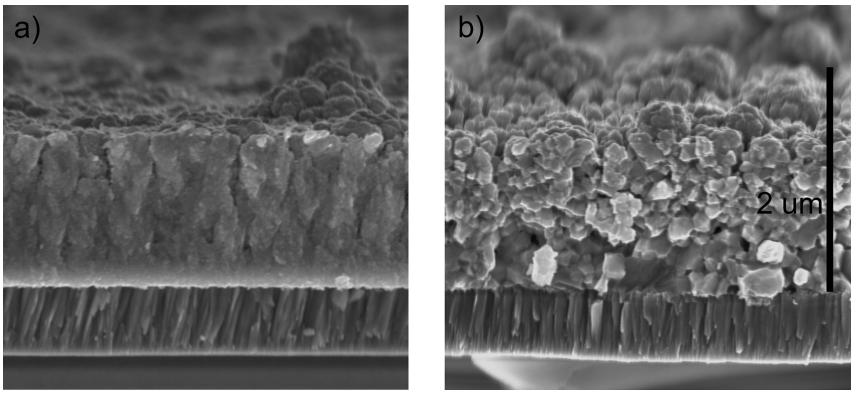

Figure 1.4 SEM images of co-deposited $CuInSe_2$: (a) precursor; (b) annealed.

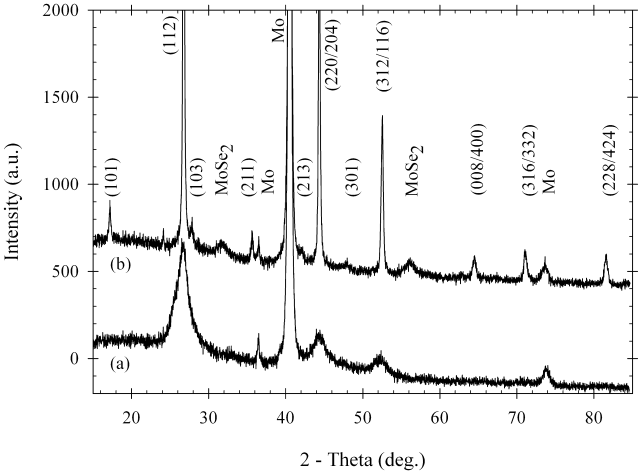

Figure 1.5 X-ray diffractogram of co-deposited $CuInSe_2$: (a) precursor; (b) annealed.

It is clear from this discussion that electrodeposition alone does not give high-quality p-type compound semiconductor layers with optoelectronic properties that are suitable for PV applications. ED therefore generally forms part of a multistage fabrication process. In the first step some or all of the elements of the semiconductor are deposited electrochemically to form a thin film, and in the subsequent steps the film is thermally annealed in an appropriate chemical environment to give it the desired properties.

1.2.2.2 **Synthetic Routes Involving Deposition and Annealing (EDA)**

The electrodeposition and annealing (EDA) route is based on recognition of the fact that ED alone has not so far proved suitable for preparing good-quality p-type compound semiconductors for PV. In the EDA process, the primary purpose of the ED step is to form a reactive precursor film that can be converted to a compound semiconductor with the desired optoelectronic properties by a process such as reactive annealing. The EDA approach increases the number of different synthetic routes to form the semiconductor. The main ED routes are (i) deposition of metal elements only, (ii) deposition of all constituent elements simultaneously in one layer, (iii) deposition of all constituent elements in two or more layers, and (iv) other hybrid methods including an ED stage. The main requirement for the electrodeposition step is to ensure that the lateral distribution of the elements is uniform. Whichever route is taken, the as-deposited films generally require annealing. The objective of the annealing step depends on the nature of the as-deposited film. For example, in the case where the electrodeposition step is used to form an alloy layer or a stack of metal layers, reactive annealing is necessary to introduce the chalcogen so as to form the desired semiconductor compound. At the other extreme, in the case where a stoichiometric semiconductor film such as CdTe has been formed by electrodeposition, annealing may be used to control the conductivity type (air anneal) or to improve crystallinity ($CdCl_2$ anneal).

1.2.2.2.1 Electrodeposition

The aim of the ED step is to provide a compact, adherent, laterally uniform precursor film with the desired stoichiometry: for commercial applications, lateral compositional uniformity needs to be guaranteed over large areas. The desired properties can only be obtained if the ED process is properly controlled. The nature of deposited layers depends on electrode material, precursor species in solution, applied potential program, hydrodynamic conditions, and temperature. For single metal systems, these factors are well understood. For deposition of multiple elements including a chalcogen, the ED process becomes substantially more complex.

The key challenges facing attempts to electrodeposit chalcogen-containing compounds are summarized below.

(i) **Substrate electrode.** The substrate electrode must be clean, preferably free of passivating oxides, and able to sustain the annealing conditions. The substrate also needs to be sufficiently conducting to minimize the potential drop so that the thickness and composition of the electrodeposit do not vary from one area to another due to the potential difference between the two areas. This is a particular problem with transparent conducting oxide (TCO) layers.

(ii) **Precursor species in solution.** The chalcogenide compounds used for absorber layers can contain from two to five elements. Metal precursor ions may be available in one or more oxidation states, each of which has different solubility and reduction potentials. The metal ion can be introduced as a salt or supplied *in situ* by anodic dissolution of a sacrificial anode. The metal ions can also be complexed with ligands to increase their solubility and prevent precipitation, particularly in alkaline solutions. Soluble chalcogen sources are more limited. H_2SeO_3 and $HTeO_2^+$ [24] are commonly used for selenium and tellurium and $S_2O_3^{2-}$ [25] for sulfur. However $S_2O_3^{2-}$ solutions tend to be rather unstable, slowly precipitating colloidal sulfur. In this case, an alternative strategy is to use organic solvents such as polyethylene glycol [26] or room temperature ionic liquids [27], which can dissolve elemental sulfur. Other components of the electroplating bath include inert supporting electrolytes, acids, bases, buffers, and organic additives. Supporting electrolytes are used to increase the conductivity of the solution to give a more uniform current distribution. An acid, base, or pH buffer is frequently added to the plating solution to control the solubility of the ionic species. Finally organic additives are used either to control reaction rates or to improve the morphology of the deposits.

(iii) **Applied potential.** Each species of ion in solution has a different reduction potential. At first sight, the simplest way to incorporate all desired species into the deposit would be to apply a sufficiently negative potential to reduce all the species. The deposits may contain the species in elemental form, but more likely in the form of binary or ternary compounds depending on the number of species in solution. The applied potential does not need to be constant: it has been shown that use of a voltage ramp can assist the incorporation of electronegative elements and reduce dendritic growth [28]. What-

ever the potential program used, the question arises – which compounds will be formed? This question is related to the mechanism of deposition, which in turn depends on the applied potential and the availability of ionic species for reduction. For the CdTe system, it is possible to electrodeposit the thermodynamically favored compound uniformly with the correct stoichiometry, but for the $CuInSe_2$ system, it is common to electrodeposit several different phases simultaneously, rather than the thermodynamically favored semiconductor, from a bath containing copper, indium, and selenium ions.

One approach to the growth of the thermodynamically favored semiconductor is based on the work of Kroger [29], who showed for chalcogenides that the reduction potential of the more electronegative element in the compound could be moved positive by an amount equivalent to the free energy of formation of the compound. This mechanism – which is equivalent to underpotential deposition – is self-limiting because the more electronegative element cannot be reduced without the presence of the chalcogen ion or chalcogen-containing compound at the electrode surface.

A common problem encountered during electrodeposition of ternary chalcogen compounds is the excess of the most noble metal (generally copper) in the deposit. To solve this problem, the concentration of the metallic precursor is either lowered in order to reduce its flux to the surface, or an organic ligand is added to complex the metal ion in order to shift its reduction potential to more negative values. Figure 1.6 illustrates this for Cu(I) ions depositing on a carbon electrode with the reduction potential shifted more negative with increasing concentration of added SCN^- ligand.

(iv) **Mass transport conditions.** The rate of electrodeposition of ions from solution is limited either by kinetics or mass transport. Kinetically limited deposition occurs when the electron transfer process from the electrode to the adsorbed ion is the rate-determining step, and mass transport-limited deposition occurs when the flux of ions to the surface is the rate-determining step. In order to obtain a uniform deposit under mass transport-limited conditions, the flux of ions to the surface must also be uniform over all parts of the electrode surface. This can be achieved in the laboratory for small areas using a rotating disk electrode (RDE), but larger areas require engineering solutions to the problem. To illustrate the problem of non-uniformity we carried out a simple copper deposition onto two molybdenum electrodes: one a stationary vertically held electrode, and the other an electrode rotated at 100 rpm. Energy dispersive x-ray (EDX) analysis at 20 keV was used to measure an approximate composition of the deposit. If the deposit has a constant thickness then the EDX measurement should return a constant compositional value for copper. Figure 1.7 illustrates the locations at which the copper composition was measured, with points 0 to 12 going horizontally and points 13 to 25 going vertically. The stationary vertical electrode has thicker layers of copper at the edges and at the bottom, consistent with an uncontrolled convection at the surface [19]. By contrast, the copper film formed on the rotated electrode shows little variation in thickness.

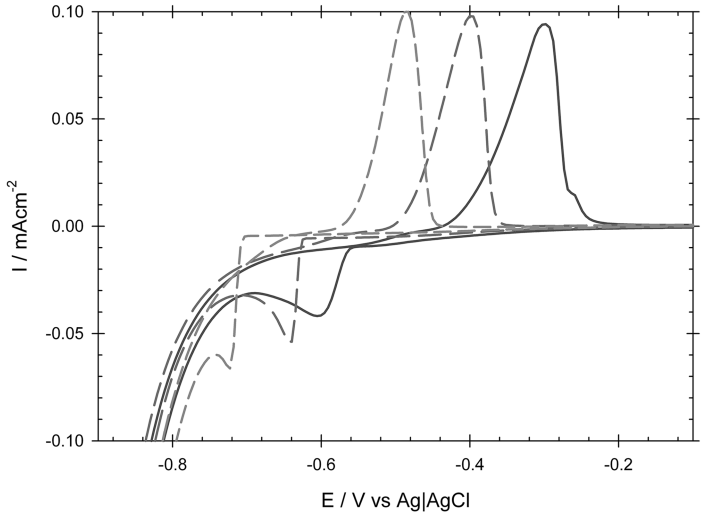

Figure 1.6 Effect of SCN^- ligand on the Cu deposition potential on carbon surface at pH 2. Solid line, 1 M KSCN; dashed line, 2 M KSCN; short-dashed line, 4 M KSCN.

(v) Temperature. Changes in temperature influence all of the kinetic and thermodynamic factors involved in electrodeposition. The deposition of CdTe, for example, is carried out at 85–90 °C. The higher temperature is necessary to obtain stoichiometric CdTe films; deposition at room temperature generally gives films that are poorly crystallized and contain excess Te. It seems probable that elevated temperatures enhance surface diffusion of adatoms so that the crystalline phase can grow properly. Metal plating is often carried out at elevated temperatures too. Generally, the optimum temperature is found empirically since the plating systems are complex with many temperature-dependent variables.

1.2.2.2.2 **Annealing**

The annealing step in the EDA process can take different forms with different purposes: (i) increasing crystallinity of the as-deposited film by allowing atoms to relax to their equilibrium positions, (ii) increasing grain size, (iii) driving solid-state reactions between two or more phases, (iv) adding or exchanging the chalcogen component, and (v) type conversion. A number of technical and safety issues have to be considered for annealing. In particular, annealing should be carried out in a closed environment to prevent release of toxic materials (Cd, Te, Se) to the environment. The heating rate, maximum temperature, and cooling rate all need to be controlled and optimized. A fast heating rate may be desirable in order to prevent formation of unwanted intermediate phases. The temperature must be sufficiently high to achieve its purpose, but it may be limited by (i) degradation of the underlying substrate and (ii) loss of volatile elements or compounds from the semiconductor film. An example of the second of these limitations is selenium loss during thermal annealing of CIGS precursor films [30]. To prevent this,

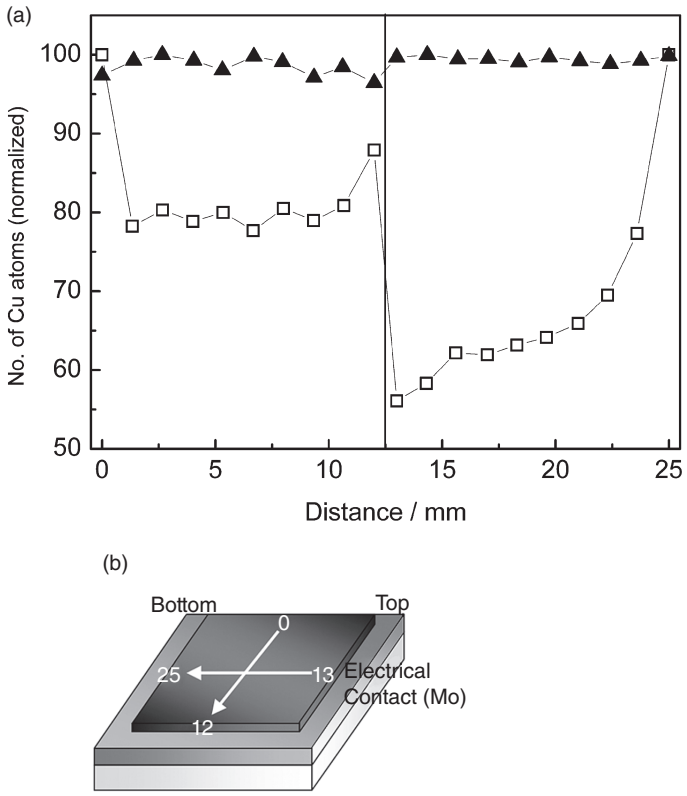

Figure 1.7 (a) Comparison of normalized copper EDX signal for electrodes with deposited copper layer. Electrodes were stationary vertical (squares) or rotated (triangles). (b) Sketch of mapped points on electrode surface for EDX measurements.

annealing is carried out in the presence of excess selenium. More generally for chalcopyrite and kesterite absorber layers, a source of chalcogen is present during the annealing process. The chalcogen can be added as an elemental solid (S, Se) which sublimes at elevated temperatures or added as the hydrogen chalcogenide (H_2S, H_2Se) in the gas phase. The atmosphere in the annealing chamber may also contain an inert gas such as argon or nitrogen, or a reducing atmosphere such as forming gas. The hydrogen in the forming gas has two roles: firstly to remove oxides, and secondly it can form the hydrogen chalcogenides from the elements *in situ*. For example Verma *et al.* showed that the formation reaction of hydrogen and selenium must be considered at 450 °C to explain the concentrations of H_2Se observed during experiments to observe its decomposition [31]. For CdTe films, a $CdCl_2$ flux can be used during annealing to induce recrystallization.

1.2.2.3 **Summary of EDA Routes**

Four distinct types of precursors that can be used for the EDA process are illustrated in Figure 1.8: (i) a stack of metal layers, (ii) an alloy of the metals, (iii) a stack of binary chalcogenides, and (iv) a layer containing all of the constituent elements

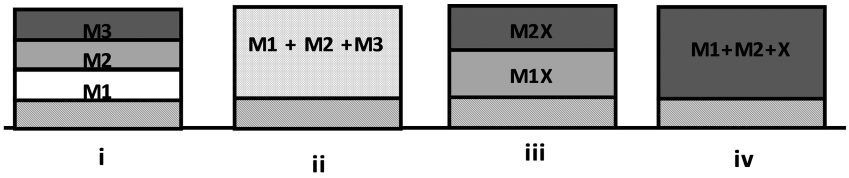

Figure 1.8 Common electrodeposited precursor types for annealing. M*n* = metal and X = chalcogen.

including the chalcogen. Approaches (i) and (ii) have been used for fabricating CIGS [32–34] and CZTS [11, 35–37, 39]. Both approaches allow for high deposition rates; for example Voss et al. [34] electroplated a Cu–In precursor in 3.5 minutes compared to a Cu–In–Se precursor that takes 60 minutes [23]. The stacked metal layer approach is the easiest in terms of plating bath chemistry but adds multiple steps and requires that each layer deposits satisfactorily on the preceding one. Some of the problems encountered in fabrication of multilayer metal stacks for kesterite synthesis are discussed in Section 1.2.3.3. The alloy approach (ii) is generally difficult since the composition is determined not only by electron transfer kinetics and mass transport but also the nature of the stable alloy phases.

The chalcogen reacts with the metal precursors during the annealing step, and the resulting semiconductors usually have large grains [34]. The disadvantages of this method are that adhesion of the semiconductor layer may be poor and that the film may contain cracks, blisters, and pinholes resulting from the substantial volume increase during the solid-state reaction.

Type (iii) precursors consist of two or more layered stacks containing binary chalcogenides. As far as we are aware, this approach has only been used for $CuInSe_2$ [28, 41, 42], although there is no reason to suppose that it would not work for other systems. The deposition of both Cu–Se and In–Se compounds is mass transport limited, and the process is complicated by the fact that several phases with different stoichiometries can be formed within a narrow range of experimental conditions (see Section 1.2.3.2.2). The binary stacks react together during annealing, inducing a phase transformation that gives rise to large grains of the ternary semiconductor compound. One advantage of this method is that there are no large changes in volume during the formation of the ternary semiconductor, but the chalcogenide deposition steps generally take longer, and the thermodynamic driving force for the reaction is not so high as in cases (i) and (ii).

Type (iv) precursors consist of a single layer containing all the necessary metals and the chalcogen(s) electrodeposited simultaneously from a single bath. CdTe [24, 43], CIS [23, 30], and CIGS [44] have all been deposited by this method. Typically the deposition of the layer is much slower than for the metal depositions due to the lower concentrations in solution. An extreme case is the deposition of CdTe, where the concentration of $HTeO_2^+$ is sub-millimolar. The deposition process is difficult to control in the case of ternary or quaternary chalcogenides, but the subsequent annealing step in the presence of excess chalcogen is used to react secondary phases and to create larger crystals of the desired absorber material.

1.2.3 EDA route to p-Type Semiconductors for Thin-Film Photovoltaics

1.2.3.1 Electrodeposition of CdTe for CdS|CdTe Solar Cells

1.2.3.1.1 Overview

II–VI (or more correctly 12,16) compound semiconductors can be synthesized electrochemically in a number of ways. In the case of sulfides, one of the simplest methods is to anodize the parent metal in an alkaline sulfide solution. This method has been used to grow films of CdS on cadmium as well as Bi_2S_3 on bismuth [45–47] for application in photoelectrochemical solar cells [46, 48–50]. Generally, however, this method is not useful for solid-state PV devices, where CdS layers are commonly deposited from a chemical bath. By contrast, cathodic synthesis of II–VI semiconductors from aqueous solutions has been developed extensively. The metal precursor is generally the M^{2+} ion, whereas the chalcogenide precursor can be thiosulfate ($S_2O_3^{2-}$) [25], selenosulfate ($SSeO_3^{2-}$) [51], or $HTeO_2^+$ [24] for sulfides, selenides, and tellurides, respectively. In the case of oxides such as ZnO, the chalcogen precursor can be molecular oxygen or hydrogen peroxide [13]. II–VI compounds have also been synthesized electrochemically from non-aqueous organic solvents [52, 53] and from ionic liquids [54]. II–VI compounds have also been synthesized by ECALE [22, 55], but this process is not suited for large-scale fabrication.

1.2.3.1.2 Historical Development

From the point of view of II–VI PV devices, by far the most important electrochemical process is the electrodeposition of cadmium telluride for CdS|CdTe heterojunction solar cells. This was the first electrodeposition process to be used in large-scale manufacture of PV devices. BP Solar's Apollo® modules, which were fabricated via an electrodeposition route, reached an advanced stage of manufacture, with a module plant coming on line in 1998. However, manufacture of Apollo modules was discontinued later, possibly as a consequence of environmental concerns. Since then, First Solar's cadmium telluride modules, which are fabricated by close space sublimation rather than electrodeposition, have achieved efficiencies of over 12%, with costs poised to fall below $1 per watt peak.

Interest in electrodeposition of CdTe goes back 30 years to the work of Panicker *et al.* [24] who established the feasibility of a process based on using an aqueous solution containing large excess of Cd^{2+} ions and Te in the form of TeO_2 dissolved in acidic solution as $HTeO_2^+$. These authors deposited CdTe on nickel and on glass coated with antimony-doped tin oxide and found that the material was n-type if pure solutions were used, whereas the presence of low-level copper impurities gave p-type layers. By 1984, Basol *et al.* [56] had reported a 9.35% efficient CdS|CdTe heterojunction cell fabricated by electrodeposition of a 60 nm CdS film onto indium tin oxide-coated glass followed by electrodeposition of the CdTe layer (1.2–1.5 μm thick). The structure was then annealed at 400 °C to convert the as-deposited n-CdTe to p-CdTe, forming the required heterojunction.

The experimental conditions used by Basol *et al.* for CdTe deposition have been followed closely in subsequent studies. The cadmium precursor consisted of 0.5 M $CdSO_4$ and the Te precursor was TeO_2 dissolved in a pH 2 electrolyte as $HTeO_2^+$ at a concentration in the range 24–40 ppm. CdTe deposition on conducting glass substrates was also studied at around the same time by Rajeshwar and coworkers [57–60]. The subsequent large-scale implementation of the electrodeposition route to CdS|CdTe solar cells was carried out by researchers at BP Solar [61, 62], culminating in the production of large-area monolithic Apollo modules with efficiencies over 10%. At this point, the development was halted, and, as a consequence, interest in electrochemical routes to CdTe solar cells has declined sharply in spite of the advantages of electrodeposition as a low-cost, low-temperature processing route. Since the electrodeposition of CdTe serves as a well-documented illustration of transferring an electrochemical process from the laboratory to a large-scale manufacturing operation, it will be examined in the following sections.

1.2.3.1.3 Mechanism of CdTe Electrodeposition

Thermodynamic aspects of cathodic electrodeposition have been discussed by Kroger [29]. The potentials for the deposition of elemental Te and Cd can be obtained from the equilibrium potentials

$$HTeO_2^+ + 3H^+ + 4e^- = Te + H_2O \quad E = 0.559 + 0.0148\log[HTeO_2^+] - 0.0443\ \text{pH} \tag{1.1}$$

$$Cd^{2+} + 2e^- = Cd \quad E = -0.4025 + 0.0295\log[Cd^{2+}] \tag{1.2}$$

Te can be reduced at more cathodic potentials to form H_2Te, and the corresponding equilibrium potential for this process is

$$Te + 2H^+ + 2e^- = H_2Te \quad E = -0.740 - 0.0295\log[H_2Te] - 0.059\ \text{pH} \tag{1.3}$$

The molar Gibbs energy of formation of CdTe is $-92\ \text{kJ mol}^{-1}$, so that CdTe can be deposited at less cathodic potentials than Cd. The relevant equilibrium potential is

$$Te + Cd^{2+} + 2e^- = CdTe \quad E = 0.074 + 0.0295\log[Cd^{2+}] \tag{1.4}$$

At more cathodic potentials, CdTe can be reduced to Cd and H_2Te. The equilibrium potential for this process is

$$CdTe + 2H^+ + 2e^- = Cd + H_2Te \quad E = -1.217 - 0.0295\log[H_2Te] - 0.059\ \text{pH} \tag{1.5}$$

These potentials effectively define the regions in which CdTe is stable to both anodic and cathodic decomposition. It can be seen that the CdTe deposition window is limited by the anodic limit of CdTe stability and by the cathodic deposition potential of bulk Cd.

The regions of stability derived from the thermodynamic analysis are shown in Figure 1.9 below a cyclic voltammogram obtained using a vitreous carbon

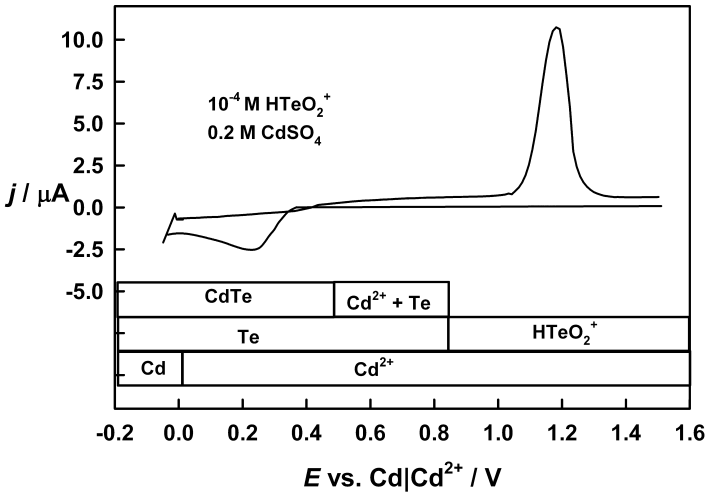

Figure 1.9 Cyclic voltammogram for deposition and stripping of CdTe at a vitreous carbon electrode in unstirred solution (pH 2, 0.2 M $CdSO_4$, 10^{-4} M $HTeO_2^+$, sweep rate 10 mV s^{-1}). The figure also shows the regions of stability of various phases. Data taken from reference [63].

electrode in an unstirred solution containing 0.5 M $CdSO_4$ and 10^{-4} M $HTeO_2^+$ at pH 2 [63]. In this case, the Cd^{2+}/Cd equilibrium potential has been chosen as a convenient zero point on the potential scale.

It can be seen from the forward sweep of the voltammogram that deposition begins around 400 mV positive of the reversible Cd^{2+}/Cd potential. This corresponds to a region where CdTe is expected to be the stable product. The beginning of Cd deposition is just evident at the cathodic limit of the voltammogram before the sweep is reversed and a well-defined anodic peak due to oxidation of the CdTe deposit is seen.

Several different mechanisms have been proposed for the electrodeposition of CdTe. Many authors have assumed that the first step is the four-electron reduction of $HTeO_2^+$ to Te followed by the reaction [64]

$$Te + Cd^{2+} + 2e^- = CdTe \tag{1.6}$$

Danaher and Lyons [65], on the other hand, assumed that the first step in CdTe deposition involves the six-electron reduction of $HTeO_2^+$ to H_2Te, which then reacts with Cd^{2+} to form CdTe, whereas Engelken and Vandoren [66] proposed that CdTe is formed as a consequence of a solid-state reaction between Cd and Te. A more detailed model involving free and occupied adsorption sites on the growing CdTe deposit was developed by Sella *et al.* [67]. The model is based on the competition for active sites between $HTeO_2^+$, Cd^{2+}, Cd, and Te. The importance of substrate–adsorbate interactions was also recognized by Saraby-Reintjes *et al.* [63], who identified slow relaxation processes during deposition of CdTe on a RDE that reflect the dynamics of adsorption processes. These relaxation processes give rise

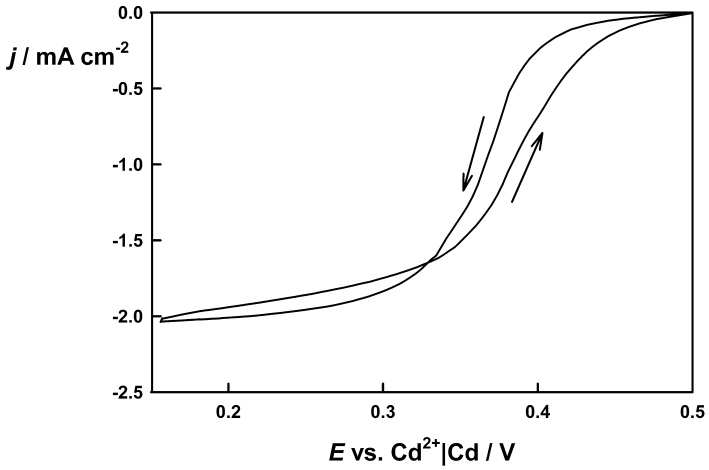

Figure 1.10 Cyclic voltammogram for deposition of CdTe at a stainless steel rotating disc electrode. Rotation rate 16 Hz, sweep rate 1 mV s^{-1}. Solution 10^{-4} M $HTeO_2^+$, 0.1 M $CdSO_4$ and 0.1 M K_2SO_4. Note the crossover between the forward and reverse sweeps that is attributed to relaxation of the surface coverages with Cd and Te species. Data taken from reference [63].

to transient behavior when the system is perturbed by applying small potential steps or steps in the rotation rate. The relaxation effects are also evident in the cyclic voltammogram for CdTe deposition at a RDE shown in Figure 1.10. The most striking feature of the voltammogram is the crossover of the cathodic and anodic sweeps which clearly has nothing to do with nucleation phenomena. Saraby-Reintjes *et al.* were able to show that this crossover is characteristic of a system in which deposition is controlled by the surface coverage of active sites. The model developed by these authors is discussed in some detail below.

A good starting point for the discussion of the mechanisms giving rise to the crossover in the voltammogram is the work of Stickney *et al.*, who developed the method known as ECALE [20–22, 68, 69]. The ECALE method relies on the fact that underpotential deposition of Cd occurs at Te surface sites, whereas Te is deposited preferentially on Cd sites. Saraby-Reintjes *et al.* assumed that stoichiometric CdTe is deposited so that, under steady-state conditions, the rate of two-electron reduction of Cd^{2+} ions at Te sites is equal to the rate of four-electron reduction of $HTeO_2^+$ at Cd sites. According to this mechanism, the Cd and Te surface coverage values self-adjust so as to maintain the 1 : 1 stoichiometric balance. The detailed model developed by Saraby-Reintjes *et al.* on the basis of these concepts predicts not only the steady-state behavior of the system but also the response of the system to perturbations in potential or mass transport (i.e., rotation rate of the RDE). The interested reader is referred to the original paper for full details. The key expression that predicts the stationary and dynamic current response relates the time dependence of the Cd coverage (θ_{Cd}) to the rates of deposition and

removal ($\vec{\upsilon}_{Cd}$ and $\overleftarrow{\upsilon}_{Cd}$, respectively) of Cd at Te sites and the rate of deposition of Te (υ_{Te}) on Cd sites (it is assumed that $\theta_{Cd} + \theta_{Te} = 1$):

$$M\frac{d\theta_{Cd}}{dt} = \vec{\upsilon}_{Cd}(1-\theta_{Cd}) - \overleftarrow{\upsilon}_{Cd}\theta_{Cd} - \upsilon_{Te}\theta_{Cd} \tag{1.7}$$

where M is a proportionality factor (mol cm^{-2}) corresponding to monolayer coverage. Solution of this differential equation shows that any step perturbation of the system will give rise to transient currents associated with readjustment of the surface coverages to their new steady-state values. The corresponding current transient takes the form

$$\Delta j = 2F[2\upsilon_{Te} - (\vec{\upsilon}_{Cd} - \overleftarrow{\upsilon}_{Cd})](\theta^0_{Cd} - \theta^\infty_{Cd})e^{t/\tau} \tag{1.8}$$

where the time constant τ that characterizes the relaxation process is given by

$$\tau = \frac{M}{\vec{\upsilon}_{Cd} + \overleftarrow{\upsilon}_{Cd} + \upsilon_{Te}} \tag{1.9}$$

Although this model is clearly simplified, it correctly predicts the signs of the current transients observed when the potential is stepped towards or away from the reversible Cd potential, mainly changing υ_{Cd}. The model also correctly predicts the sign of the transient current response to changes in the rotation rate of the RDE, which mainly perturbs υ_{Te}. Most convincingly of all, it predicts that there will be a crossover in the cyclic voltammogram when the term in square brackets is equal to zero. The main limitation of the model is that it does not take into account changes in surface area of the CdTe film during deposition.

1.2.3.1.4 Structural Properties of Electrodeposited CdTe Layers

A number of factors control the structural properties of electrodeposited CdTe. Good-quality near-stoichiometric crystalline material is obtained by deposition at 85 °C onto CBD CdS films on FTO-coated glass (CdTe films can also be grown on FTO-coated glass that has been "sensitized" by previous cathodic reduction [70], but generally they are of lower quality). The deposits exhibit preferential orientation along the <111> axis, with the strongest texturing observed for films deposited close to the reversible $Cd^{2+}|Cd$ potential [70]. The strong preferential orientation and the quality of the deposit can be seen in Figure 1.11 which shows a high-resolution transmission micrograph of a CdTe deposit on a CdS substrate. The stacking faults that are evident as dark/light bands are also seen in high-quality epitaxial layers of CdTe grown from the vapor phase.

The very high quality that can be achieved for the cathodic deposition of CdTe is illustrated by the work of Lincot *et al.* [71], who showed that epitaxial layers of CdTe can be grown electrochemically on the $(\bar{1}\bar{1}\bar{1})$ surface of single-crystal InP. Perfectly oriented films could be produced by pre-depositing a thin (20–30 nm) buffer layer of epitaxial CdS on the InP. Figure 1.12 illustrates the RHEED pattern observed for a 0.12 µm CdTe film on InP, demonstrating a high degree of epitaxy, with the CdTe growing with no rotation of the crystallographic directions in the basal (111) plane.

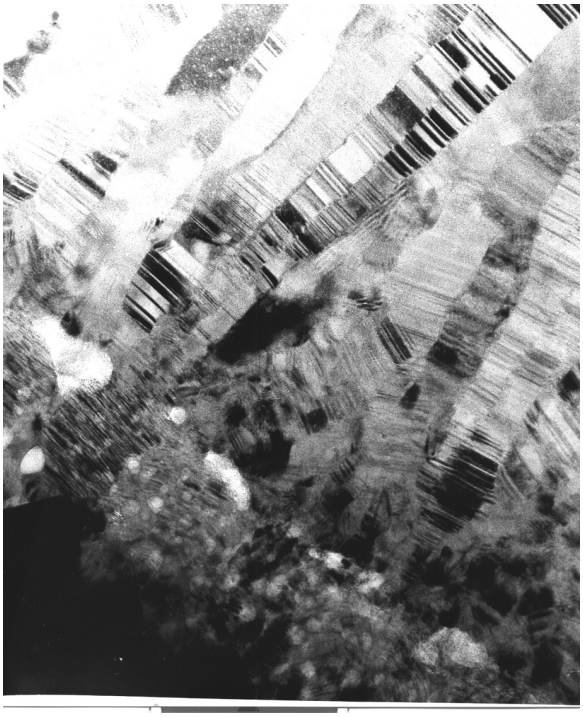

Figure 1.11 High-resolution TEM image of electrodeposited CdTe film showing columnar structure and stacking faults. Daniel Lincot.

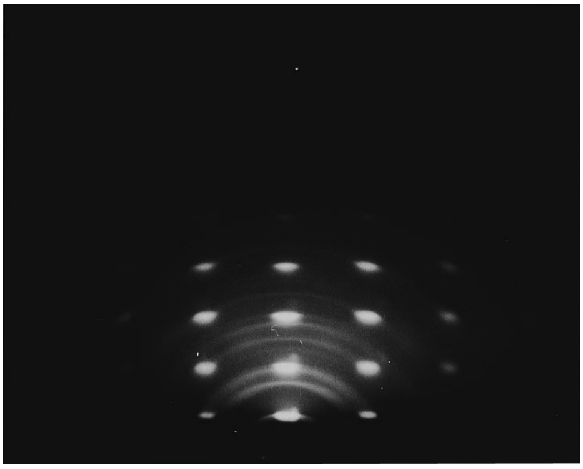

Figure 1.12 RHEED of electrodeposited CdTe on InP/CdS. The substrate is oriented in the [112] azimuth. Daniel Lincot.

1.2.3.2 Electrodeposition of CIGS for CIGS|CdS|ZnO Solar Cells

1.2.3.2.1 Historical Perspective

The first report of a $CuInSe_2$/CdS heterojunction solar cell – based on single-crystal $CuInSe_2$ – appeared in 1974 [72]. The cell achieved an efficiency of 5%. In 1983 the first electrochemical approach to produce a polycrystalline thin film of $CuInSe_2$ was reported by Bhattacharya [73] in which Cu, In, and Se were deposited simultaneously from an acidic solution. Other approaches to the synthesis of polycrystalline $CuIn(S,Se)_2$ thin films appeared quickly after the first report: for example, Hodes *et al.* annealed an electrodeposited Cu–In alloy [74], Kapur *et al.* annealed stacked Cu–In layers [75], and Bhattacharya *et al.* annealed In–Se Cu–Se stacks [28]. The EDA routes which currently produce the most efficient $CuIn(S,Se)_2$ solar cells involve co-deposition of all of the constituent elements [76] followed by annealing in a sulfur atmosphere, and the electrodeposition of a Cu–In alloy with a small amount of Se, again followed by annealing in sulfur [34]. Both routes produce devices with around 11% power conversion efficiency.

Over a series of many articles stretching from 1994 (Guillemoles, Lincot and Vedel [77]) through to the present day (Chassaing *et al.* [78]), the ENSCP group in Paris have studied the mechanisms for the simultaneous three-element electrodeposition of $CuInSe_2$. These detailed investigations have shown that the deposition mechanism is complicated and time dependent, but current understanding is sufficiently good to be able to control the process so as to yield solar cells with 11.5% efficiency via the EDA route [76].

In order to compete with the high efficiencies of cells fabricated using physical vapor deposition [7], it is necessary to optimize the bandgap of the materials by incorporating Ga with a controlled concentration profile. Ga incorporation in ED films was first achieved by Calixto *et al.* in a co-deposition of all elements [79]. The best electrochemically incorporated Ga-containing devices have been reported by Kampmann *et al.* [33] who achieved a device efficiency of over 10% by using a stacked layered approach.

1.2.3.2.2 $Cu(In,Ga)Se_2$ via Stacked Metal Layers

As described in Section 1.2.3, CIGS can be formed by annealing thin films of the metal elements in a chalcogen atmosphere: the Showa–Shell–Siemens industrial process is based on this route [80, 81]. Whether a stack of metals or an alloy layer is used depends in part on the annealing process. Single-element depositions are easier to control, but an alloy deposition reduces the number of deposition steps.

Copper salts are available in the +1 or +2 oxidation state, while the stable In and Ga oxidation states are +3. The relevant standard reduction potentials are given below.

$$Cu^{2+} + 2e^- = Cu \quad E = 0.34 - RT/2F \ln[aCu^{2+}] \tag{1.10}$$

$$In^{3+} + 3e^- = In \quad E = -0.34 - RT/3F \ln[aIn^{3+}] \tag{1.11}$$

$$Ga^{3+} + 3e^- = Ga \quad E = -0.53 - RT/3F \ln[aGa^{3+}] \tag{1.12}$$

Copper salts are reasonably soluble over a wide pH range, but In and Ga salts only exhibit solubilities above 1 mM at pH < 3 for In^{3+} and at pH < 1.5 for Ga^{3+} [82]. Rotating disk electrode experiments show that Cu deposits under mass transfer-controlled conditions on Mo, whereas In deposits under kinetic control at room temperature. There are a few reports on electrodeposition of Cu/In or In/Cu stacks for the realization of CIS semiconductor compounds [83, 84]. One technologically interesting report from Penndorf *et al.* [83] describes the use of copper tape as both the substrate and source of Cu for the formation of $CuInS_2$. Indium was electrodeposited on the copper tape in a roll-to-roll process with remarkably high current densities of 150–200 mA cm^{-2} with the help of thiourea. Cell efficiencies of up to 6% were reported with this approach.

One recent route taken in our laboratories is the electrodeposition of stacked Cu/In/Ga layers on Mo followed by annealing in a Se/forming gas atmosphere. Each layer is deposited from a separate plating bath: details of the baths and deposition conditions are given in Table 1.1. The basic Cu plating bath was adapted from Barbosa *et al.* [84] with the addition of a zwitterionic surfactant that reduces grain size and surface roughness [11]. A basic Cu bath is used because the Mo substrate is passivated by a surface oxide in acidic conditions, leading to poorly adherent films. The indium plating bath is adapted from the review paper of Walsh and Gabe [85]. Different Ga plating baths have been tried with different organic ligands to enhance the solubility of Ga(III) at reasonable pH values. The ligands glycine, KSCN, and ethylenediaminetetraacetic acid have been tested in both basic and acidic media. The Ga plating bath with glycine at pH 13 is found to give reasonable deposits of Ga on Cu surfaces with 57% plating efficiency (measured by integrating the charge of a forward and reverse cyclic voltammogram), but on an In surface the plating efficiency is found to be less than 10%, as measured by inductive coupled plasma mass spectrometry.

Table 1.1 Typical plating recipes for Cu/In/Ga stacked layer deposition.

Element	Solution	E_{dep} vs. Ag|AgCl (V)	Rotation speed (rpm)
Cu	0.1 M $CuCl_2$ 3 M NaOH 0.2 M sorbitol 0.25 µg l^{-1} Empigen BB	–1.20	150
In	0.261 M $InCl_3$ 2.3 M H_3NO_3S 2.0 M NaOH 8.0 g l^{-1} dextrose, 2.29 g l^{-1} triethanolamine	–0.95	0
Ga	0.1 M $Ga_2(SO_4)_3$ 3 M NaOH 0.5 M glycine	–1.70	100

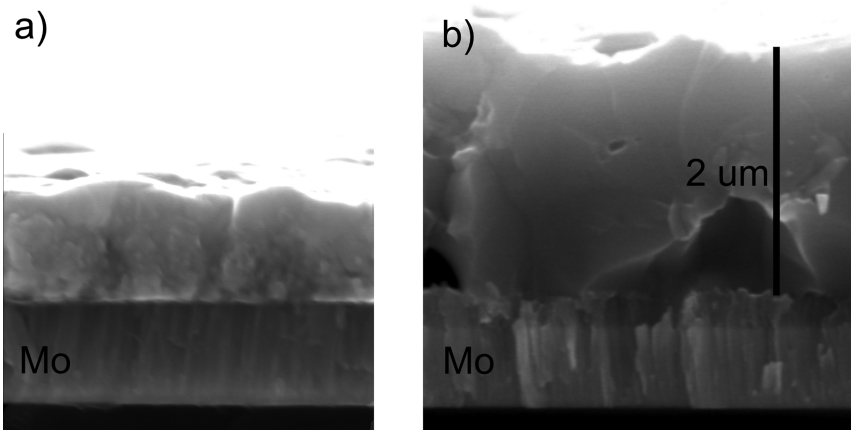

Figure 1.13 SEM images of (a) Cu/In/Ga stacked precursor and (b) annealed precursor.

The substrates used for the deposition were 1 inch square Mo-coated glass pieces held in a RDE with contacts at the corners. Rotation was used to ensure lateral thickness uniformity across the entire sample. The separate layers of a deposited Cu/In/Ga stack are not visible in the SEM image of Figure 1.13a, possibly due to alloying. The stack was annealed in a mixture of forming gas and selenium vapor, and the resulting crystalline semiconductor layer is shown in Figure 1.13b. The annealing process has formed large crystals of CIGSe, and some voids can be observed at the interface.

The annealed $CuInSe_2$ films are p-type and give reasonable photocurrent responses when tested in an electrolyte (see Section 1.3). However, to date device performance has been poor, about 4%, which we attribute to large pinholes in the films, and some blistering. Investigations are under way to determine if this is a function of the annealing or of the electrodeposition.

Kampmann *et al.* [86] have successfully deposited layers in this manner, albeit with a thermally evaporated Se capping layer on the Cu/In/Ga stack. In their case no details are given due to the industrial nature of the work, but device efficiencies of 10.4% are reported [86].

To successfully deposit elemental Ga with high rates the hydrogen evolution reaction must be suppressed by using organic additives. Some suitable additives and conditions for suppressing hydrogen evolution are discussed in the following sections.

1.2.3.2.3 **Cu(In,Ga)Se_2 via Metal Alloys**

Hodes *et al.* [74] plated Cu–In alloys on titanium substrates at pH 2 using aqueous $CuSO_4$, $In_2(SO_4)_3$ (or $InCl_3$), and H_2SO_4 at a potential of –1.0 V vs. standard calomel electrode (SCE). These alloy films were annealed in a 1 : 1 H_2S : argon mix for 30 minutes. Annealing at 400 °C produced only sphalerite (cubic) phases while at 500–550 °C the chalcopyrite (tetragonal) phase dominated and grain size increased.

Hodes *et al.* suggested that this was due to quasi-rheotaxy type of crystalline growth. The films annealed at the higher temperatures also showed higher photoactivity.

The most significant work on the alloy route has been published by the Attotech–Erlangen collaboration in a series of papers [34, 87–90]. Attotech – a company specializing in electroplating – developed a Cu–In alloy plating bath that allowed deposition of precursor layers in 3.5 minutes [34]. Unfortunately no details of the chemical composition of the plating bath are available, but it evidently contains complexants and brightening and wetting agents. Additionally the plating bath contained a very small amount of Se, equivalent to less than 5% of the necessary chalcogen – presumably to promote adhesion to the Mo substrate. Voss *et al.* [34] demonstrated that the Cu/In ratio was constant when the hydrodynamic conditions were varied from 3 to 10 rad s^{-1} and the applied potential was varied by 300 mV. This relative insensitivity to experimental conditions is important, since there can be a substantial lateral variation of potential across large-area substrates due to the iR drop. Furthermore Voss *et al.* found that the Cu/In ratio could be varied from 0.8 to 1.6 by adjusting the pH from 2.8 to 3.5. Uniform electrodeposits on areas of 30 × 30 cm were achieved using a spray nozzle array to control the hydrodynamic conditions. XRD analysis of the deposited precursors showed the expected $Cu_{11}In_9$ and $CuIn_2$ phases, but no selenide phases were observable due to the very small amount of Se in the precursor. When annealed in a mixed S and Se atmosphere, the precursor converted into the semiconductor $CuIn(S,Se)_2$; no additional phases were observed by XRD. The best final cells fabricated by Voss *et al.* had a power conversion efficiency of 11.4% equaling the efficiencies achieved by vacuum deposition techniques for $CuIn(S,Se)_2$ [91].

Friedfeld *et al.* deposited a $CuGa_2$ alloy phase consisting of 0.5 μm isolated grains from a 5 M NaOH metal sulfate bath using a RDE [92]. A layer of $CuInSe_2$ was then added in a one-step electrodeposition, and the combined layer was annealed to form CIGS. The In/Ga ratio could be varied by varying the relative thicknesses of the two layers, as evidenced by the shifting cell lattice parameters obtained by XRD.

Zank *et al.* co-deposited In and Ga potentiostatically onto 10 cm^2 Cu-coated Mo using a 2.1 M KCN bath in 0.5 M KOH with 62 mM dextrose [32]. Cyanide is a very strong complexing agent for cations in solution, but also appears to bind to the electrode surface to suppress the hydrogen reaction and reduce the electron transfer rate. As a consequence, the deposition is kinetically limited, which eliminates the need to control the mass transport. Films containing approximately 60% Ga could be deposited at very negative potentials, and the Ga content increased with increasing negative potential up to the limit of solvent breakdown. Interestingly the morphology of the deposit was found to depend on the Ga content. When a Ga content of 35.7% was deposited, the layer was in a liquid phase, as the alloy is a liquid below at the deposition temperature. The Ga reacts with the Cu phase underneath and forms the $CuGa_2$ phase.

Kois *et al.* took this approach one step further and co-deposited Cu–In–Ga simultaneously from a 0.4 M acetate bath (pH 5) containing 50 mM metal ions and

2 M KSCN [93]. With these conditions, the bath was stable and the reduction of the SCN ligand was not observed. Cu and In deposition were found to be hydrodynamically controlled, while Ga deposition was found to be unaffected by stirring. Metal precursors containing variable amounts (from 2 to 30 at%) of Ga could be made by altering the stirring in the bath. Precursors annealed in Se vapor exhibited a broadened (112) peak demonstrating mixed $CuInSe_2$ and $CuGaSe_2$ phases rather than just one phase.

1.2.3.2.4 Cu(In,Ga)Se_2 via Stacked Binary Layers

The deposition of the binary selenide phases is discussed in this section in the order Cu–Se, In–Se, and Ga–Se followed by a summary of some recent results from our laboratory on the stacking and annealing of Cu–Se/In–Se stacks.

Massaccesi *et al.* [94] studied in detail the room temperature deposition of copper selenide films onto rotating disk tin oxide electrodes from deoxygenated solutions at pH 2.45 containing 1 mM $CuSO_4$, 0.1 M K_2SO_4, and between 0 and 10 mM H_2SeO_3. Two Se(IV) species are present at this pH, and their reduction potentials are given below.

$$H_2SeO_3 + 4H^+ + 4e^- = Se + 3H_2O \quad E = 0.741 - 0.0391pH + 0.0148\log(H_2SeO_3) \tag{1.13}$$

$$HSeO_3^- + 5H^+ + 4e^- = Se + 3H_2O \quad E = 0.778 - 0.0739pH + 0.0148\log(H_2SeO_3^-) \tag{1.14}$$

Massaccesi *et al.* studied the deposition of copper and selenium separately and then co-deposition of the two elements. Copper deposition on tin oxide was found to be facile, but selenium appeared to passivate the electrode surface, and no limiting current was observed in a linear voltammogram. However, limiting currents for selenium could be observed when the tin oxide electrode was replaced with a copper electrode. Co-deposition on tin oxide was studied using voltammetry in solutions containing 1 mM Cu and variable amounts of H_2SeO_3. It was observed that copper deposits at less negative potentials than selenium, which is the reverse of what their standard potentials suggest (see Equations 1.10, 1.13, and 1.14). Furthermore the addition of selenium to the copper solution did not move the copper reduction potential more positive, as would be expected for the Kroger underpotential deposition mechanism [29]. To explain the observed voltammograms and the compositional stoichiometry of the deposits, Massaccesi *et al.* defined the ratio of Cu to Se fluxes (r_J) at the surface of the electrode as

$$r_J = \frac{J_{Cu}}{J_{Se}} = \left(\frac{D_{Cu}^n}{D_{Se}^n}\right)\frac{[Cu]^{sol}}{[Se]^{sol}} \tag{1.15}$$

where $J_{[X]}$ is the limiting current, $[X]^{sol}$ is the concentration of ions in the bulk, and n is the exponent of the diffusion coefficient which is equal to 2/3. For films deposited between potentials of –0.5 and –0.8 V vs. a mercury sulfate electrode (MSE, +0.64 V vs. SHE), it was found that the composition of the deposit was directly proportional to the flux ratio r_J, suggesting that the copper and selenium

reduce independently of voltage and one another. At potentials more negative than –0.8 V vs. MSE, only Cu_2Se was formed. Massaccesi *et al.* found that if the flux of Se(IV) ions is higher than that needed for the formation of Cu_2Se, Se(I) and Se(II) species were formed which diffuse back into solution and reduce the H_2SeO_3 to form red colloidal Se(0):

$$H_2SeO_3 + 2H_2Se \rightarrow 3Se + 3H_2O \tag{1.16}$$

Massaccesi *et al.* calculated phase maps showing the species present as a function of r_J and applied voltage. The complexity of the deposition process is illustrated by the calculations for $r_J = 0.8$, when the following species are formed at the electrode surface going from positive to negative potentials: Cu, Cu_2Se, Cu_3Se_2, CuSe, Se(0), Se_2^{2-}, Se^{2-}.

Lippkow and Strehblow [95] studied the effect of temperature on copper selenide deposition from an electrolyte similar to that used by Vedel *et al.* and found that the Cu_2Se phase was preferred when deposition was carried out at 80 °C, whereas a mixed phase of Cu_2Se and $CuSe_2$ was formed at lower temperatures.

The first detailed study of the electrodeposition of In_2Se_3, onto tin oxide RDE, was reported by Massaccesi *et al.* [96], who used a bath containing 2 mM $In_2(SO_4)_3$, 1 mM H_2SeO_3,with 100 mM K_2SO_4 as background electrolyte adjusted to pH 3.5 with 10 mM H_2SO_4. Again, as for the Cu–Se case, the authors examined the deposition of the elements individually first and the co-deposition second. At room temperature H_2SeO_3 was reduced to Se(0), passivating the surface of the electrode producing a red deposit, while at 82 °C a gray deposit was formed that was consistent with the gray conducting allotrope of selenium. On the cathodic sweep, indium deposition could not be readily distinguished from the reduction of the tin oxide electrode. Co-deposition of both elements at room temperature yielded a passivated electrode at potentials equal to or more positive than –1.05 V vs. MSE and a gray conducting In–Se phase at more negative potentials. At potentials more negative than –1.05 V vs. MSE, H_2SeO_3 is reduced to H_2Se when no indium is present in the solution. Therefore it appears at room temperature that In(III) only deposits in the presence of H_2Se. When insufficient In(III) is available at the surface, the H_2Se reacts with H_2SeO_3 to form Se(0) (1.16). However, at 82 °C, strongly adherent gray films containing a Se/In ratio similar to that of In_2Se_3 were successfully deposited at –1.05 V vs. MSE. Annealing the films in vacuum at 390 °C crystallized the films into photoactive n-type β-In_2Se_3.

Bhattacharya *et al.* [28] successfully deposited In_2Se_3 at room temperature using much higher concentration baths than Massaccesi *et al.*: the baths contained 25 mM $In_2(SO_4)_3$ and 25 mM H_2SeO_3 at pH 1.5. These authors recommended plating a 50 nm thin Cu film on the Mo substrate to improve adhesion and observed that an In-rich film can be obtained by replacing $In_2(SO_4)_3$ by $InCl_3$ in the deposition bath.

Aksu *et al.* [97] have deposited In–Se compounds from basic solutions containing complexing agents such as tartrate and citrate. The deposition solutions consisted of $InCl_3$, H_2SeO_3, and 0.7 M complexing agent, and the pH was adjusted with NaOH. For basic solutions, the predominant Se(IV) ion in solution is SeO_3^{2-}, with the reduction potential given below:

$$SeO_3^{2-} + 6H^+ + 4e^- = Se + 3H_2O \quad E = 0.875 - 0.0886pH + 0.0148\log[SeO_3^{2-}] \tag{1.17}$$

Thus, the SeO_3^{2-} reduction potential is more negative in basic solutions and therefore closer to the reduction potential of In(III) (1.11). Aksu *et al.* showed that they could control the In/Se ratio from 4/7 to 9/1. Furthermore using this approach of complexing agents, and exchanging $InCl_3$ for $GaCl_3$, they also managed to deposit Ga–Se compounds, but only in a narrow range of pH between 7 and 8.5.

In our laboratory we have recently prepared In_2Se_3 films at 82 °C for use in In_2Se_3/Cu–Se precursor stacks for converting into $CuInSe_2$. Initially the recipe of Massaccesi *et al.* [96] was employed, but later the deposition bath was modified by inclusion of a pH 2 buffer, and deposition was carried out under controlled hydrodynamic conditions. The buffer was introduced to control pH better at the electrode surface, and also a thin underlayer of copper was deposited onto the molybdenum substrate to reduce the initial hydrogen evolution. The cyclic voltammograms for a stationary and a rotated electrode are shown in Figure 1.14. For the stationary working electrode, a H_2SeO_3 to Se(0) reduction peak is observed on the forward scan at –0.4 V vs. Ag/AgCl followed by a poorly defined peak due to the deposition of an indium selenide phase. Hydrogen evolution is observed at potentials more negative than –0.6 V vs. Ag/AgCl. On the return sweep a small anodic stripping peak is observed at –0.6 V vs. Ag/AgCl. For the RDE at 250 rpm, the initial current density is more than double the stationary current density, and again the H_2SeO_3 to Se(0) reduction peak is observed at –0.4 V vs. Ag/AgCl. In this case no distinct In–Se reduction peak is evident. On the reverse sweep, the current remains similar to the forward sweep, decreasing at about –0.5 V vs.

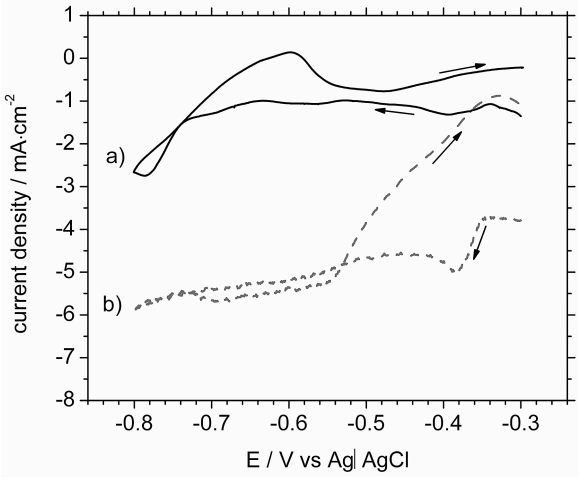

Figure 1.14 Cyclic voltammogramms for 1 mM H_2SeO_3 and 2 mM $In_2(SO_4)_3$ buffered at pH 2 at 82 °C. Scan rate 10 mV s^{-1}. RDE with a 100 nm Cu layer plated on Mo substrate. (a) 0 rpm, (b) 250 rpm.

Ag/AgCl, to indicate where In–Se deposition ceases to be possible. It was found that stoichiometric In_2Se_3 could be deposited at fixed potentials more negative than –0.6 V vs. Ag/AgCl and selenium-rich layers at potentials more positive than this.

Deposition on 1 inch square substrates without hydrodynamic control was found to give non-homogeneous films with visible variation in the color and light-scattering properties. EDX measurements confirmed differences in composition and layer thickness across the film. By contrast, smooth and uniform reflective gray films were obtained when the deposition was performed under controlled hydrodynamic conditions, and EDX measurements confirmed uniform thickness and stoichiometry. SEM images comparing the deposits formed on the vertical stationary deposit and on the rotated electrode are shown in Figure 1.15. The rotated substrates produce very compact uniform layers of indium selenide, while the non-rotated substrates produce a nodular type of growth.

It is known that $CuInSe_2$ can be formed by reacting Cu–Se and In–Se phases [98, 99]. The Gibbs free energy change for this reaction is –49 to –120 kJ mol^{-1} depending on the stoichiometry of the two binary compounds [100]. The potential benefits of this reaction as a route to the final product include recrystallization of the layers in the absence of large lattice changes since the chalcogen is already present. Guillen and Herrero [41] electrodeposited Cu/In_2Se_3 stacks and observed better recrystallization during the annealing of the stacks (compared to co-deposited elements) as shown by the narrowing of the main $CuInSe_2$ XRD peaks.

In_2Se_3/Cu_xSe_y stacks have been electrodeposited and annealed by Hermann *et al.* [101]. Additionally this group has managed to incorporate gallium into an indium gallium selenide layer by using solutions saturated in chloride ions to stabilize the gallium [102].

In our own laboratory, we have prepared laterally uniform $In_2Se_3/Cu–Se$ stacks and annealed them in a forming gas/elemental selenium atmosphere. Firstly In_2Se_3 layers were deposited at 400 rpm on 10 nm thick copper underlayers (see above). The copper selenide phase was then deposited on top of the In_2Se_3 at room temperature from an electrolyte containing 5.5 mM H_2SeO_3, 2.6 mM $CuCl_2$, 236 mM LiCl, and a pH 3 buffer comprising sulfamic acid and potassium

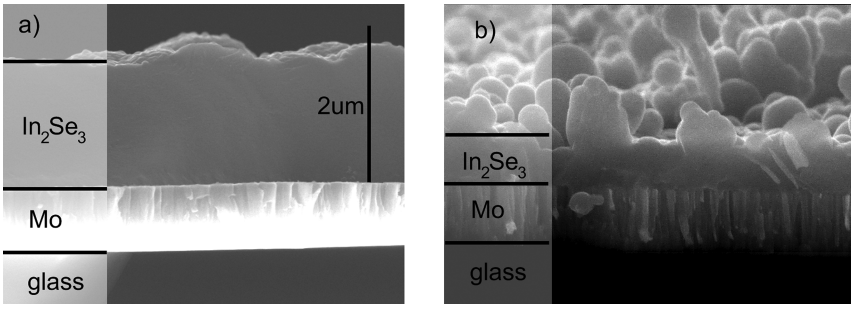

Figure 1.15 SEM images of In_2Se_3 deposits on thin Cu-coated Mo substrates rotated at (a) 250 and (b) 0 rpm.

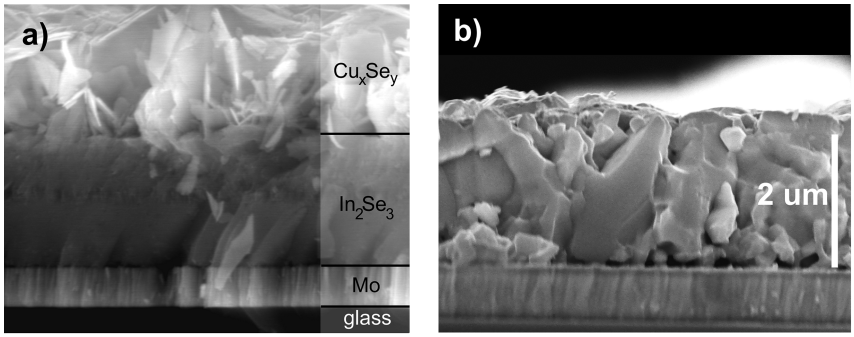

Figure 1.16 SEM images of binary selenide stack: (a) precursor; (b) annealed.

biphthalate. The deposition was carried out at –0.30 V vs. Ag/AgCl on a RDE at 100 rpm. The resulting Cu/Se ratio of the layer was 0.75 as measured by ICPMS, indicating a mixture of CuSe and Se(0) phases were present, in agreement with Thouin *et al.* [103]. Figure 1.16a shows an SEM image of the precursor and Figure 1.16b of the annealed sample. The two distinct metal selenide phases are observable in the precursor, and the recrystallization of both the layers is clearly evident in the annealed layer: large grains extending from molybdenum surface to the top of the layer can be seen in the SEM image. XRD clearly shows that only the $CuInSe_2$ phase is present. Using the photoelectrochemical tests described in Section 1.3, it was found that the layer is p-type doped with only a small photoresponse.

1.2.3.2.5 Cu(In,Ga)Se_2 via Simultaneous Deposition of All Elements

Simultaneous co-deposition of all elements is the widely reported route for the formation of CIGS semiconductor layers or their precursors. Simultaneous electrodeposition of three or four elements is more complicated than deposition of the binary selenides. The main problems are (i) the large differences in standard reduction potentials and (ii) the fact that copper deposition is diffusion controlled. Three main approaches have been taken to tackle these problems, namely use of controlled hydrodynamic conditions, the use of organic additives to change reduction potentials, and pulse plating. All three approaches are discussed in this section, starting with $CuInSe_2$ for simplicity and then considering CIGS.

One of the first detailed investigations into the mechanism for co-depositing $CuInSe_2$ was conducted by Mishra and Rajeshwar, who used cyclic photovoltammetry and a RRDE as investigative tools [104]. They used a simple metal sulfate bath containing SeO_2, with the pH adjusted to 1.0 using sulfuric acid. Comparing Cu–Se and In–Se systems at room temperature, they observed that the In–Se system was kinetically much slower than the Cu–Se system, even though the concentration of In(III) was an order of magnitude larger than that of Cu(II). They found that indium incorporates into the copper selenide phase at potentials lower than the In–Se deposition potential. Cyclic photovoltammetry was carried out using chopped white light. On the forward scan in the three-element solution, the

first two peaks were attributed to the formation of $Cu_{2-x}Se$, and no photoresponse was observed. Between the third and fourth reduction peaks, a cathodic p-type photoresponse, attributed to the formation of $CuInSe_2$, was observed. Mishra and Rajeshwar proposed the following mechanism for the incorporation of indium into the deposit:

$$Cu_{2-x}Se.H_2Se_{(adsorbed)} + In^{3+} = CuInSe_2 + 2H^+ + (1-x)Cu^+ \quad (1.18)$$

The key point in this proposed mechanism is that $Cu_{2-x}Se$ needs to be present on the surface together with the adsorbed H_2Se.

The Vedel group studied the co-deposition under three different conditions [105, 106]. They used solutions similar to those employed for their study of the Cu–Se binary system [94, 103] with the addition of 1 mM In(III). Again the key parameter of importance is the ratio of the fluxes of copper and selenium in solution. Vedel *et al.* define α which is just the reciprocal of r_J (Section 1.2.3.2.4) or the flux ratio of Se(IV) ions to Cu(II) ions incident on the surface [105]. They found that when α was less than two, it was possible to deposit mixtures of $CuInSe_2 + Cu_2Se$ or of $CuInSe_2 + Cu$. When α was greater than two, $CuInSe_2 + In_2Se_3$ was obtained. It was proposed that in the presence of In(III), Se(IV) could be more easily reduced to Se(II). In further work, the same authors found that having an excess of In(III) in solution allowed them to control the compounds deposited on the electrode surface. Furthermore they developed a phase map which is shown in Figure 1.17 [106].

The latest work from the Paris laboratory is that of Chassaing and co-workers [78, 107–109], who investigated the deposition of $CuInSe_2$ onto a Mo RDE from a

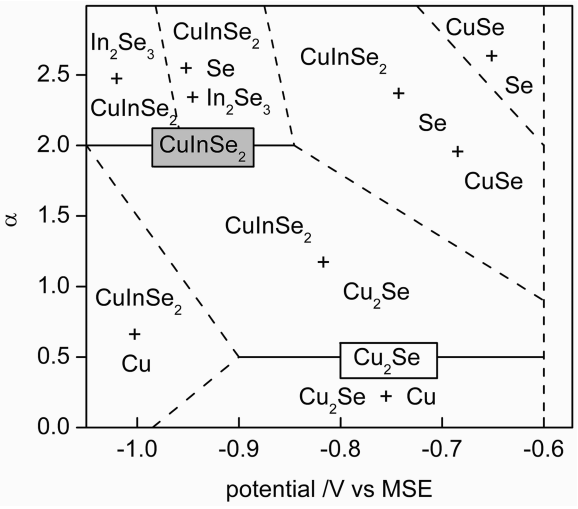

Figure 1.17 Electrochemical phase diagram showing the composition of co-deposited films. Parameter α is the flux ratio of Se(IV) and CU(II) ionic species to the surface. MSE is a mercury sulfate electrode (MSE, +0.64 V vs. NHE) [106]. Reproduced by permission of The Electrochemical Society.

sulfate solution containing 1 mM Cu, 1.7 mM selenous acid, and 6 mM In(III) adjusted to pH 2. They investigated the deposition process *in situ* as a function of time by polarization and impedance spectroscopy, and *ex situ* by chemical, XPS, and XRF analysis. Using these values of concentration and the diffusion coefficients from [94] a value for α of around 2 or slightly higher was obtained depending on the value of n used, and single phase $CuInSe_2$ could be obtained with the correct applied potential. Depositions were carried out at various potentials for fixed amounts of time. At –0.9 V vs. MSE after 3 seconds of deposition there were $10^{11}\,cm^{-2}$ nuclei approximately 10 nm in diameter formed on the molybdenum surface, consisting mainly of copper and selenium. After the first 10 seconds, the Se/Cu surface ratio tended to a value of 2, while at longer times the ratio tended to 3. At deposition times longer than 10 seconds the In/Cu ratio at the surface was just 0.5 while in the bulk it was 1.0. XPS data showed that the selenium on the surface of the films was a mixture of Se(0) and Se(II) oxidation states. Furthermore when depositing below potentials of –0.6 V vs. MSE Chassaing *et al.* [78] observed deposits of binary Cu–Se phases as well as elemental Se(0). For deposition at potentials more negative than –0.6 V vs. MSE, no elemental Se(0) was seen in the deposits, but incorporation of indium into the Cu–Se phases occurred – a process that became more pronounced at more negative potentials. Impedance data showed that at potentials just positive of –0.6 V vs. MSE, the deposited layer was highly capacitive due to the presence of Se(0) on the surface, whereas the capacitance fell at more negative potentials due to the formation of the semiconducting $CuInSe_2$ phase. Chassaing *et al.* [107] proposed the following reaction scheme based on their results:

$$2Cu^{2+} + H_2SeO_3 + 8e^- + 4H^+ = Cu_2Se + 3H_2O \tag{1.19}$$

$$H_2SeO_3 + 4e^- + 4H^+ = Se(0)_{(adsorbed)} + 3H_2O \tag{1.20}$$

$$Cu_2Se + 3Se(0)_{(adsorbed)} = 2CuSe_{2(surface)} \tag{1.21}$$

$$CuSe_{2(surface)} + In^{3+} + 3e^- = CuInSe_2 \tag{1.22}$$

Equation 1.20 requires that Se(0) is absorbed onto a deposition surface containing Cu_2Se. When sufficient Se(0) is available it is then consumed to form $CuSe_2$ at the surface which has been shown to be the site where In reacts to form the $CuInSe_2$ chalcopyrite compound [109]. This proposed mechanism requires, of course, that the electrode surface should be continually refreshed in Cu_2Se and Se.

One of the more successful co-depositions of CIGS was reported by Calixto *et al.* [110], who used a ratio of selenium and copper ions in the deposition bath similar to that employed by Chassaing *et al.*, but chose a chloride-based supporting electrolyte to stabilize the Ga(III) ions. These authors achieved a Ga/(Ga + In) ratio of 0.2 in the precursor film as indicated in the XRD analysis of the annealed semiconductor by the shift of the (112) peak from d = 3.348 to 3.314 Å. The best device had an efficiency of 6.2%. Bhattacharya *et al.* also used similar routes to co-deposit CIGS and incorporated additional Ga into the deposit by non-electrochemical means [111].

Ligands or complexing agents have been used to try and reduce the dependence of the electrodeposited precursor stoichiometry on applied potential and solution composition. Kemell *et al.* [112, 113] showed that a constant composition close to the required 1 : 1 : 2 for $CuInSe_2$ was achieved over a 300 mV potential range using a SCN ligand. The deposition bath contained 0.01 M CuCl and $InCl_3$, 1 mM SeO_2, and 2 M KSCN. Higher concentrations of KSCN resulted in the deposited films containing traces of the SCN ligand. Using this approach, photoactive p-type $CuInSe_2$ was obtained after annealing. Other popular ligands include citric acid, chloride ions, triethanolamine, and ethylenediaminetetraacetic acid – see Lincot *et al.* [30] and references therein.

Pulse plating, the application of a cyclic potential program to the work electrode, has been used to deposit $CuInSe_2$ precursor films from a pH 2 chloride bath with a ratio of Cu to Se ions of 1 : 2 in an unstirred solution [114]. Nomura *et al.* found that smooth stoichiometric precursors could be obtained by the application of two potentials of –0.7 and 0 V vs. SCE with a duty cycle of 33%.

1.2.3.3 CZTS

The ternary compound CZTS is currently being investigated as an indium-free alternative to CIGS in thin-film solar cells. Bandgaps between 1.36 and 1.62 eV have been reported for CZTS, making the material suitable for a single-junction solar cell [10, 115]. CZTS films show p-type behavior with doping levels that are suitable for thin-film devices [35, 116, 117]. Photovoltaic devices are generally fabricated by the same methods used for CIGS cells, except that the CIGS layer is replaced by CZTS. The current record device, with a reported AM 1.5 efficiency of 6.7%, was prepared by a two-stage process involving preparation of a co-sputtered precursor using Cu, ZnS, and SnS targets followed by annealing in H_2S [10]. Single-stage co-evaporation methods, which produce the best devices for CIGS, have yielded efficiencies up to 4.2% [118].

There are currently two basic approaches to fabricate CZTS layers by electrodeposition. In the stacked elemental (SEL) approach, the parent metals are electrodeposited sequentially to form a stack [35, 119] which is then annealed in a sulfur atmosphere to from CZTS. In an alternative approach, the parent metals are co-deposited to form a mixed metallic or alloy layer which is then annealed in the presence of sulfur [120, 121]. Both approaches have yielded cells with AM 1.5 efficiencies of over 3%.

1.2.3.3.1 Fabrication of Thin-Film Solar Cells via the SEL Method

The SEL approach has some advantages over co-deposition, because it allows simpler coulometric control of the precursor stoichiometry. The SEL method may also be more suitable for large-scale fabrication since there is no requirement to balance the deposition rates of several different metals, so higher current densities can be used. If an alloyed precursor is preferred for the sulfur annealing step, a short (<5 min) heat treatment at 200–350 °C is sufficient to completely alloy the stacked precursor. In this section, we highlight some of our recent work on the fabrication of CZTS solar cells by the SEL route [11].

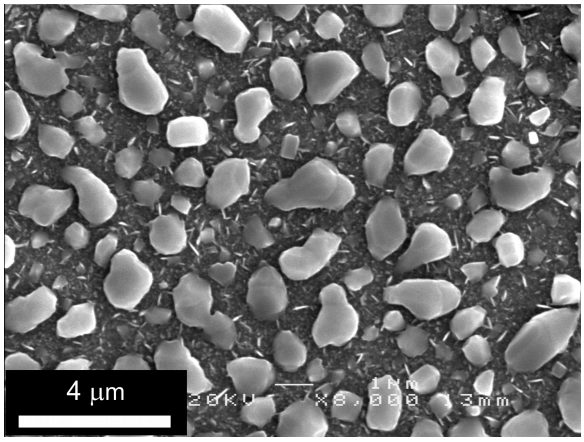

Figure 1.18 SEM image of Sn deposited on Cu using sorbitol bath [123]. Reproduced from [11].

Earlier work in our laboratory encountered problems with non-uniform thickness and incomplete coverage [35–37]. The morphology of the Sn layers in particular was poor with large islands as shown in Figure 1.18 [36, 122].

Figure 1.19a illustrates the problem of poor microscopic morphology in the case of a CZTS film prepared from a Cu/Sn/Zn precursor with the island structure shown in Figure 1.18. The sulfurized CZTS film contains small grains, and the morphology is uneven. Figures 1.19b and 1.19c show elemental distribution maps for Sn and Zn over the same area. The contrast variations in the two elemental maps are not coincident, suggesting that the film contains other phases besides CZTS. These variations probably arise from the island morphology of the Sn layer in the precursor seen in Figure 1.18, which was not laterally homogenized during sulfurization.

In later work in our laboratory, thickness variations in the precursor layers were eliminated by carrying out electrodeposition under hydrodynamic control using a RDE [122]. In addition the electrodeposition processes and stacking order were modified to improve the precursor morphology. The improved Cu/Sn/Cu/Zn stacks were sulfurized and converted into devices, the best of which showed an efficiency similar to that reported by Araki *et al.* [120] and Ennaoui *et al.* [121] for CZTS devices fabricated using metal co-deposition routes. Electrodeposition was carried out potentiostatically in three-electrode mode onto square 25×25 mm Mo-coated soda-lime glass substrates mounted in the face of a cylindrical polypropylene RDE which was placed face-down in the electrodeposition solution and rotated during deposition. The deposition conditions used for growth of the sequential metal layers are given in Table 1.2. Deposition efficiencies were obtained from ICP-MS measurements of dissolved films. The precursors were placed with 100 mg of sulfur inside a graphite container in a tube furnace filled to 500 mbar with 10% H_2 in N_2 and heated to 575 °C for 2 hours. Prior to device fabrication and materials characterization, the sulfurized films were etched in aqueous KCN

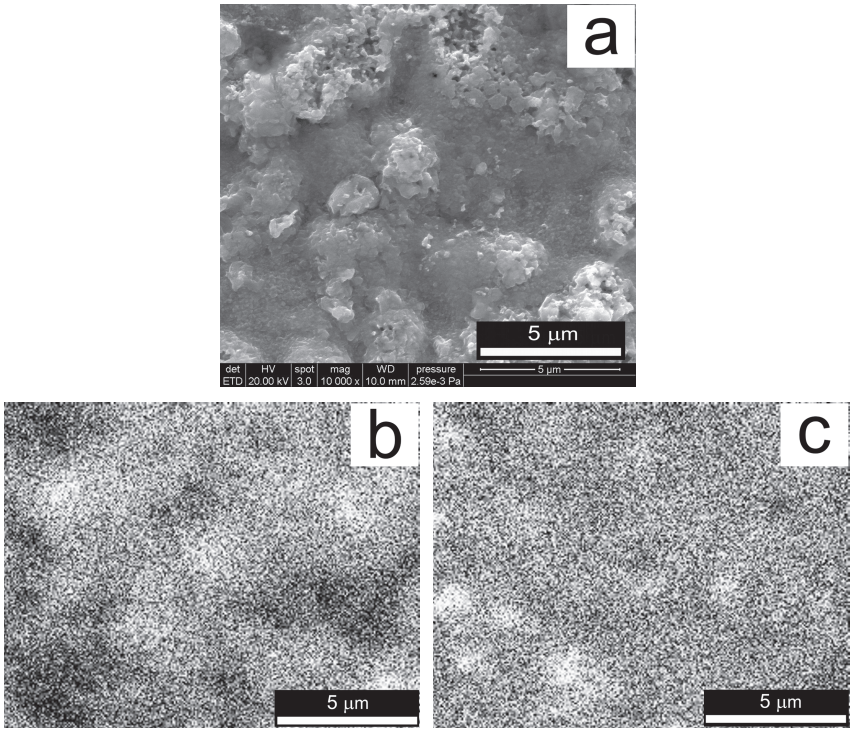

Figure 1.19 (a) SEM image of a sulfurized Cu/Sn/Zn precursor stack and EDX element distribution maps of (b) Sn and (c) Zn from the same area as (a). Reproduced from [11].

Table 1.2 Chemical composition and electrodeposition parameters for each layer of the Cu/Sn/Cu/Zn precursor. Potentials are given with respect to the Ag|AgCl reference electrode.

Layer	Composition of electrolyte	*E* (V)	Rotation (rpm)
Cu	3 M NaOH, 0.1 M $CuSO_4$, 0.2 M Sorbitol, 0.9 mM Empigen BB (surfactant)	–1.20	150
Sn	50 mM $Sn(SO_3CH_3)_2$, 1 M CH_3SO_3H, 3.6 mM Empigen BB	–0.72	100
Zn	0.1 M $ZnSO_4.7H_2O$, pH3 hydrion buffer, 0.5 M K_2SO_4	–1.20	150

to remove copper sulfide phases. Devices were fabricated by deposition of a CdS layer by CBD followed by deposition of i-ZnO and Al:ZnO layers by sputtering. Contact to the cells was made by a nickel grid. Following fabrication, devices were heated in air at 200 °C for up to 5 minutes.

Growth of Copper Layers Nucleation and growth of metal layers on the Mo-coated soda-lime glass substrates is not without problems. In acidic conditions, the untreated Mo surface is passivated by an oxide layer [82] that prevents effective nucleation of Cu, resulting in non-adherent, powdery deposits. Adhesion can be improved by sensitizing the substrate with Pd prior to electrodeposition [119]. Since the oxide layer on Mo is soluble in alkaline media, surface passivation can be avoided, and excellent Cu layer deposits can be obtained using an RDE in an alkaline Cu electrolyte adapted from the work of Barbosa *et al.* [84]. Introduction of a quaternary ammonium surfactant (Empigen BB) to the electrolyte improves the morphology of the Cu deposit.

Growth of Tin Layers Tin layers deposited in our previous work [122] from the alkaline sorbitol electrolyte consisted of large crystals with low nucleation density, giving incomplete coverage. Much improved flat layers showing specular reflectivity were obtained using a methanesulfonic acid electrolyte containing Empigen BB. The film morphology of the tin layer produced in this electrolyte is shown in Figure 1.20, where it is the underlying layer.

Growth of Zinc Layers The morphology of the Zn layer is strongly influenced by the structure of the underlying Sn layer. Although excellent Zn films could be grown on Cu layers, nucleation of Zn on Sn layers was found to be very uneven. A comparison of the voltammetric behavior of $Zn^{2+/0}$ at Sn and Cu electrodes (Figure 1.21) shows that underpotential deposition (UPD) of Zn on Cu occurs due

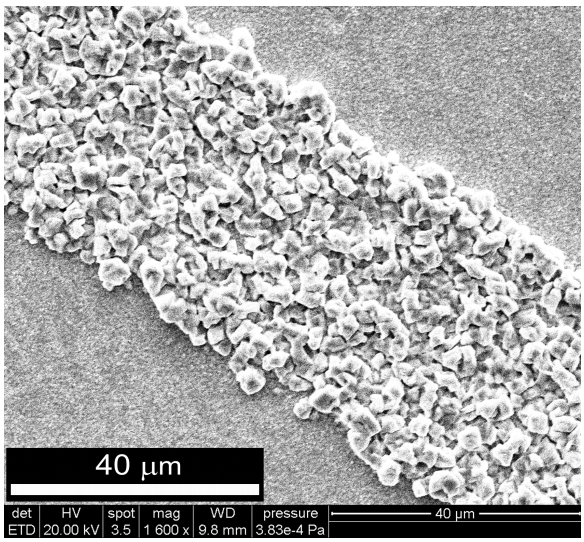

Figure 1.20 SEM image of Zn deposit on Sn layer deposited from a methanesulfonic acid electrolyte. Reproduced from reference [11].

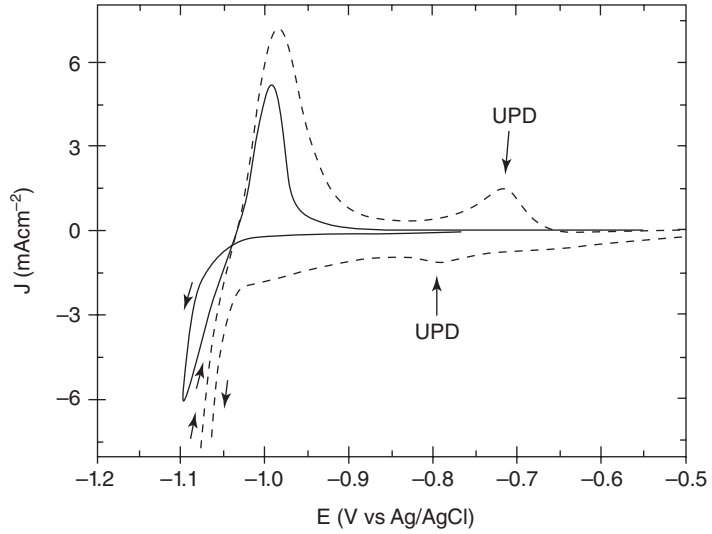

Figure 1.21 Cyclic voltammogram for $Zn^{2+/0}$ at Sn (solid line) and Cu (dashed line) surfaces. Reproduced from reference [11].

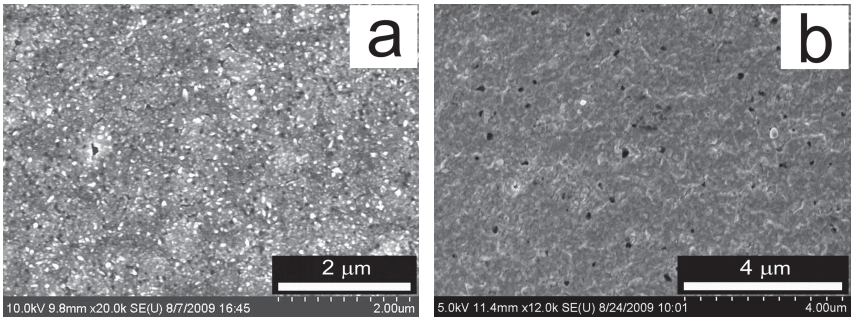

Figure 1.22 SEM images of (a) Cu layer deposited onto Sn and (b) Zn deposited onto Cu. Reproduced from reference [11].

to the energetically favorable formation of a Cu–Zn alloy. This UPD layer completely covers the Cu surface in a thin layer of Zn, strongly inhibiting hydrogen evolution. By contrast, no UPD of Zn on Sn was observed and hydrogen evolution interferes with Zn deposition and nucleation is non-uniform.

This problem was solved by depositing a second Cu layer on top of the Sn film, using a negative potential to inhibit displacement of Sn^{2+} from the film. It was found that good Zn films could grown on top of this intermediate Cu layer to give a Cu/Sn/Cu/Zn stack. Figure 1.22 shows the morphology of the second Cu layer and the final Zn layer. This arrangement of the layers may be advantageous since Araki *et al.* reported that a precursor stack in which Cu and Sn were neighbors gave the best devices after sulfurization [124]. This observation is consistent with the reaction scheme proposed by Hergert and Hock [125], which describes

the growth of CZTS as proceeding via intermediate formation of Cu_2SnS_3 and ZnS [126].

Characteristics of Stacked Precursor Films The new Cu/Sn/Cu/Zn precursors have good lateral uniformity, and the layers consist of small compact grains. The EDX maps in Figure 1.23 show the macroscopic uniformity of the precursor stacks over a 1.4 cm^2 area, in terms of the compositional ratios Cu/(Zn + Sn) and Zn/Sn. Both show only small variations, significantly better than those achieved previously [122]. In the example shown, the Cu/(Zn + Sn) ratio was 0.80 ± 0.02 and the Zn/Sn ratio was 1.37 ± 0.05.

The XRD diffractogram (Figure 1.24) measured 14 days after preparation of the stacked layer precursor indicates that the metal layers have alloyed partly at room temperature, even though there are no visible changes in color or texture. The only elemental phase observed is Cu, with binary Cu–Sn and Cu–Zn phases accounting for the remaining peaks. No ternary phase is observed, in agreement with the findings of Chou and Chen [127], whose study of the Cu–Sn–Zn system at 250 °C showed only binary phases.

SIMS measurements on the precursor confirm intermixing of the layers occurs at room temperature (Figure 1.25). In particular, the Cu signal is clearly seen in both the Sn and the Zn phases. The majority of the Zn is still confined to the top of the precursor, while the Sn is distributed towards the bottom, suggesting it is mainly diffusion of Cu that is responsible for alloy formation.

Characterization of Annealed CZTS Films Sulfurization of the Cu/Sn/Cu/Zn precursor stacks gave better microscopic uniformity than the previous Cu/Sn/Zn stacks. An SEM image and EDX maps of the Sn and Zn distributions in a film produced from the Cu/Sn/Cu/Zn precursor stack is shown in Figure 1.26. A comparison with Figure 1.23 shows a much more uniform distribution of the elements for the film formed from the four-layer stack precursor. The high degree

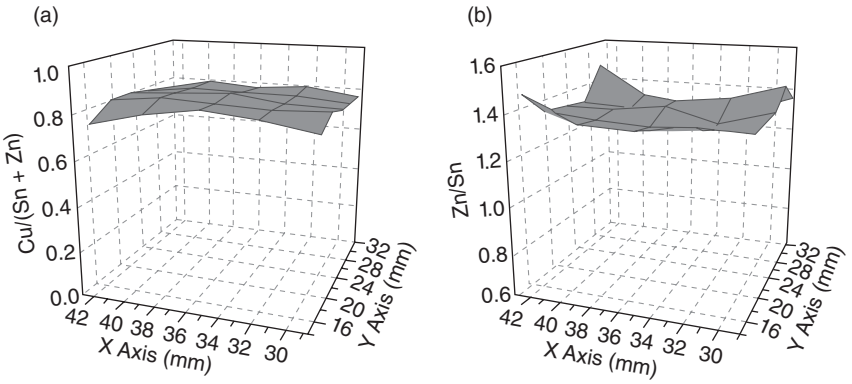

Figure 1.23 Large-area EDX maps of a Cu/Sn/Cu/Zn precursor stack in terms of the ratios (a) Cu/(Zn + Sn) and (b) Zn/Sn. Reproduced from reference [11].

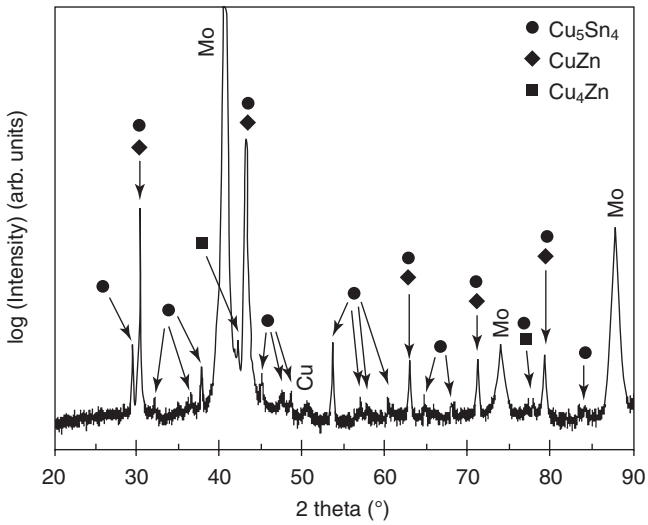

Figure 1.24 XRD spectra of a stoichiometric Cu/Sn/Cu/Zn precursor stack deposited on Mo. Reproduced from reference [11].

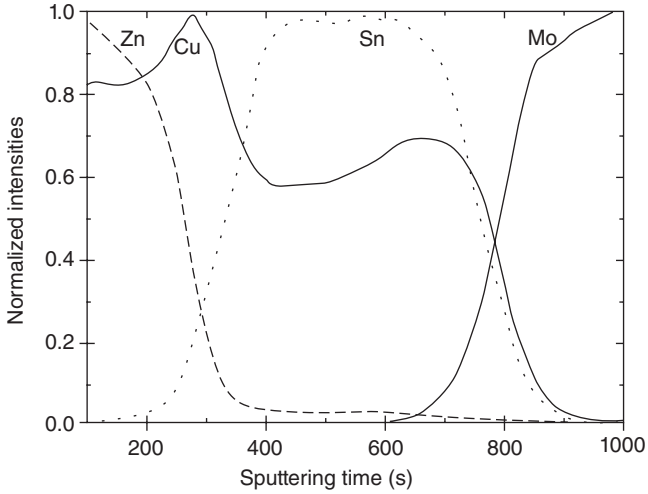

Figure 1.25 SIMS depth profile of Cu/Sn/Cu/Zn precursor layer after four weeks at room temperature. Each element has been normalized to its highest value. Reproduced from reference [11].

of correlation between the two elements suggests that the films are single phase. It appears that the only published study of the phase diagram of the Cu_2S–ZnS–SnS_2 system is by Olekseyuk *et al.* [128], who have reported that Cu_2ZnSnS_4 only exists as a single phase over a very small range of composition varying by less than ±1.5% absolute from the stoichiometric values for each element. The CZTS film in Figure 1.26 has a Cu/(Zn + Sn) ratio of 0.70 ± 0.07 and a Zn/Sn ratio of

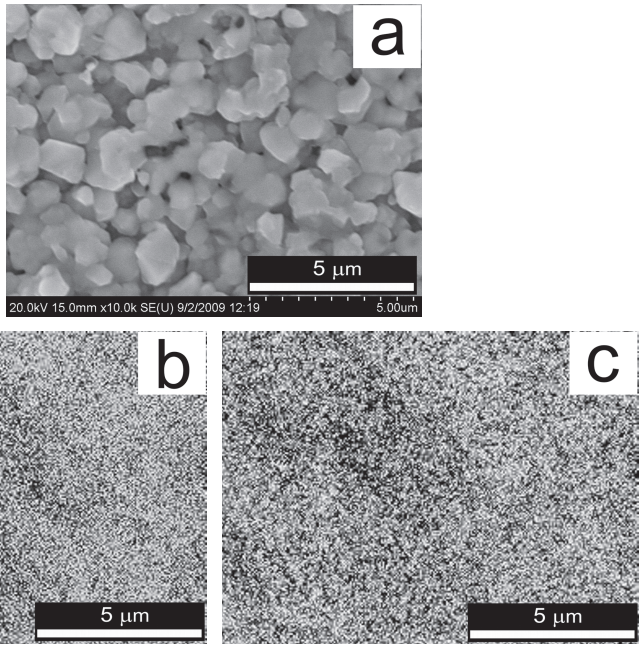

Figure 1.26 (a) SEM image of a sulfurized Cu/Sn/Cu/Zn precursor stack. (b) Sn and (c) Zn elemental EDX maps corresponding to (a). Reproduced from reference [11].

1.06 ± 0.12. Both values lie outside the single-phase region suggested by Olekseyuk *et al.*, but no significant secondary phases could be distinguished within the layer with the resolution of mapping used here.

A grazing incidence XRD spectrum of a sulfurized film is shown in Figure 1.27. All reflexes can be assigned to the kesterite structure using ICSD card 01-075-4122 (inorganic crystal structure database) except for two peaks (labeled with asterisks) that are assigned to a copper sulfide phase. This assignment is supported by the fact that the two peaks disappear when the film is etched in aqueous KCN. The figure also shows the largest reflexes for the most probable secondary phases, ZnS and Cu_2SnS_3. It is important to note that these phases have very similar unit cells to CZTS, and are essentially indistinguishable from it using XRD.

1.2.3.3.2 **CZTS Solar Cells**

Several cells were fabricated using the CZTS layers. Figure 1.28 shows a cross-sectional image of the best cell showing that the CZTS layer near the Mo substrate consists of small grains with some voids, whereas the upper part is formed of large close-packed grains of around a micron in size. This kind of structure is also observed for $CuInSe_2$ films prepared by a similar electrodeposition–annealing approach [87].

SIMS measurements were made on the best cell, after removal of the ZnO and CdS layers: the results are shown in Figure 1.29. The concentration of all three

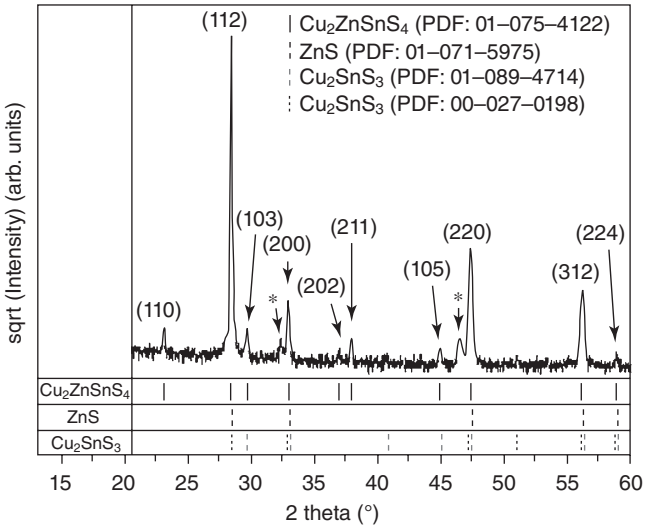

Figure 1.27 Grazing incidence XRD pattern of sulfurized Cu/Sn/Cu/Zn precursor layer. The asterisks indicate a secondary phase assigned to copper sulfide. Cu/(Zn + Sn) = 0.70 ± 0.07, Zn/Sn = 1.06 ± 0.12. Reproduced from reference [11].

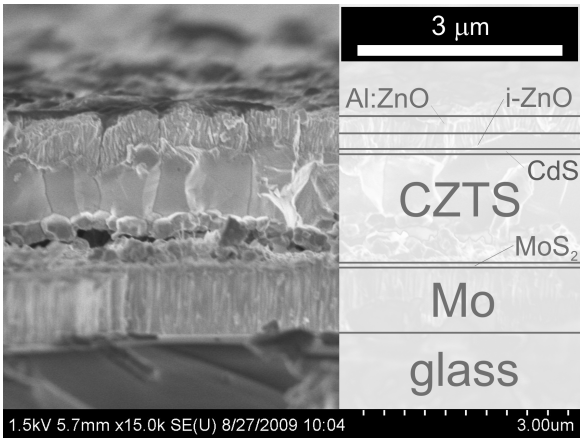

Figure 1.28 SEM image of a cross section through the best performing cell. Reproduced from reference [11].

metallic elements is constant throughout the bulk of the film. The CZTS film appears to be slightly Cu and Zn deficient at the front interface. The S concentration is also uniform throughout the depth of the film, increasing slightly at the front of the film, possibly due to the presence of residual CdS.

The best device gave an open circuit voltage (V_{oc}) of 480 mV, a short circuit current density (J_{sc}) of 15.3 mA cm^{-2}, and a fill factor of 45%. The corresponding power conversion efficiency was 3.2%, which is similar to the values reported by Araki *et al.* (3.16% [120]) and Ennaoui *et al.* (3.4% [121]).

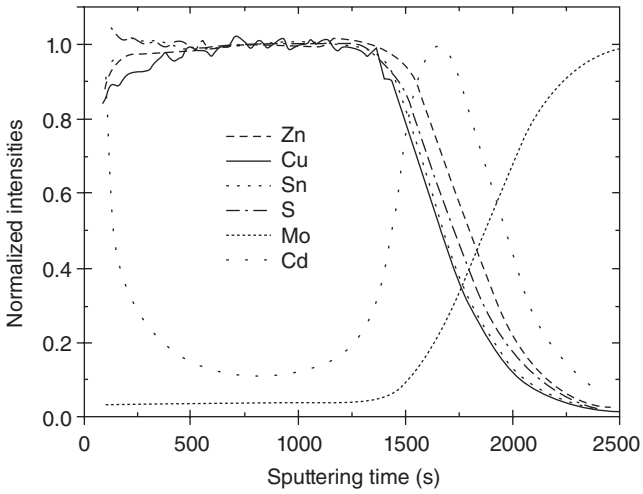

Figure 1.29 SIMS profile of the best performing cell after chemical removal of the ZnO and CdS layers. Each element has been normalized to its highest value. Reproduced from reference [11].

This section has shown that improvements in the microscopic and macroscopic uniformity of electrodeposited stacked elemental layer precursors and the use of a four-layer stack–Cu/Sn/Cu/Zn–result in better solar cells. Clearly CZTS has some way to go before it can compete with CIGS, but these early results are certainly encouraging.

1.2.4 Future

Electrodeposition of CIS and CIGS absorber films has been realized from aqueous solution, but all of the precursor films suffer from a number of problems. The incorporation of In and more especially Ga is not trivial. Due to their limited solubility and large negative reduction potentials close to the hydrogen evolution reaction of water, it is necessary to use strong complexation chemistry, involving toxic ligands such as cyanide and to work under highly alkaline conditions to avoid hydrogen evolution which causes uncontrolled stirring and poor morphology of the deposits. Moreover, In and Ga are often deposited together with their oxide or hydroxide forms under these conditions. Nevertheless, the electrodeposited precursor layers are transformed into device-quality CIGS during the highly energy consuming post-annealing step under Se atmosphere at high temperature.

A possible solution to these problems could be to replace the aqueous deposition media by room temperature ionic liquids (RTILs). These are defined as liquids consisting of molecular cations and anions that have a melting point below 100 °C. Due to the size of the molecular ions and the fact that the charge is delocalized through the molecule, these liquids have large electrochemical windows. Another potential benefit is that RTILs have high degradation temperatures and low vapor

pressures, allowing them to be used at temperatures up to 250 °C. These wide electrochemical and thermal windows allow processes which are impossible in aqueous or organic solvents.

The electrochemical window of water varies between 1 and 2 V, while those of most common pyrrolidinium-based ionic liquids are between 5 and 6 V [129]. Shivagan *et al.* [130] have shown that In and Ga can be reversibly electrodeposited from a eutectic-based ionic liquid composed of a 1:2 choline chloride:urea mixture. El Abedin *et al.* [131] have investigated the electrochemistry of Cu, In, and Se individually in the ionic liquid 1-butyl-1-methylpyrrolidinium-bis(trifluoromethylsulfonyl)amide. More recently, the same group showed that Ga can be deposited electrochemically and electroless on Au(111) electrodes [132]. The very low vapor pressure of ionic liquids allows them to be used as electrodeposition media at elevated temperatures, thus being potentially interesting to improve the crystallinity of the deposited thin films. Two reports from the literature mention the effect of temperature on the deposition of compound semiconductors from ionic liquids. Yang *et al.* [133] showed that for the electrodeposition of InSb from 1-ethyl-3-methylimidazolium chloride/tetrafluoroborate, at temperatures up to 120 °C, the crystallinity of the deposit increased with the deposition temperature. The as-deposited films were p-type and photoactive. Hsiu *et al.* [134] deposited CdTe thin films at constant potential at temperatures up to 140 °C onto glassy carbon, titanium, and tungsten substrates from 1-ethyl-3-methylimidazolium chloride/tetrafluoroborate.

From the very limited literature describing ED of compound semiconductors from ionic liquids it can be seen that more research is needed to understand the fundamental aspects of ED from these liquids. However it is reasonable to conclude that due to their unique electrochemical and thermal properties, ionic liquids are likely to play an important role in the field of compound semiconductor electrodeposition. Ongoing work in our laboratories is investigating controlled gallium incorporation and high-temperature electrodeposition of CIGS thin films from ionic liquids.

1.3
Characterization of Solar Cell Materials using Electrolyte Contacts

1.3.1
Overview

The electrochemical and photoelectrochemical properties of semiconductors in contact with electrolytes have been widely studied using single-crystal samples as well as polycrystalline thin films, and several excellent general books are available in the literature [135–138]. By contrast, the scope of this section is relatively narrow since it focuses specifically on practical applications of electrolyte contacts for the purpose of characterizing thin-film solar cell layers and partially completed PV devices of various kinds.

The main advantage of using electrolyte contacts to characterize the semiconducting layers that are used in PV devices is that liquid contacts are transparent and easily removed without damaging the material. Furthermore, provided that the semiconductor is stable in the electrolyte used, liquid contacts tend to be rather ideal since they avoid the lattice mismatch problems and chemical interactions that are often encountered with metal contacts. Formation of a Schottky barrier at the semiconductor–electrolyte junction allows convenient variation of the band bending in the space charge region by controlling the electrode potential with respect to a reference electrode potential. For measurements under illumination, where minority carriers are driven to the interface, the electrolyte generally contains a suitable scavenger species to prevent anodic or cathodic photodecomposition of the semiconductor. This section describes the main semiconductor characterization techniques that employ electrolyte junctions. A recent comprehensive survey of experimental techniques in semiconductor electrochemistry by Peter and Tributsch [5] contains useful background information about the techniques described here.

1.3.2 The Semiconductor–Electrolyte Junction

Basic aspects of the semiconductor–electrolyte junction are discussed in the references given in the previous section. Here we summarize the main points, placing particular emphasis on their relevance to the characterization of thin-film PV materials. For further details on semiconductor characterization in general, the reader is referred to the excellent book by Schroder [139].

If an inert electrolyte (i.e., one not containing a redox system) is used to form a semiconductor–electrolyte contact, the potential distribution at the interface is determined by the applied electrode potential. When the semiconductor is held at the *flatband potential*, there is no space charge in the semiconductor, and therefore the conduction and valence bands are flat. For characterization purposes, the junction is usually polarized so as to create depletion conditions where a space charge region is formed in the semiconductor as majority carriers are withdrawn from the junction. This corresponds to reverse biasing a conventional Schottky junction. For n-type materials, polarization to more positive electrode potentials corresponds to reverse bias, whereas the polarization direction is the opposite for p-type materials. Provided that the material is not highly doped, the current flowing under depletion conditions in the dark is small, although in practice pinholes and defects in polycrystalline layers give rise to higher currents than those observed with single crystals. Polarization of the semiconductor–electrolyte junction into accumulation is best avoided since this is likely to lead to decomposition reactions involving majority carriers: n-type materials will be reduced and p-type materials will be oxidized. These decomposition reactions can modify the semiconductor surface substantially, complicating characterization measurements.

When a semiconductor is illuminated under depletion conditions with light of sufficient energy ($h\nu > E_g$, where E_g is the bandgap), electron–hole pairs are created

and minority carriers (electrons for p-type and holes for n-type material) move to the interface where they can take part in electron transfer reactions, generating a photocurrent. In the case of n-type materials, the photocurrent is anodic, whereas for p-type materials it is cathodic.

If a redox electrolyte is used, equilibration of the electron free energies in the semiconductor and electrolyte phases at open circuit results in the alignment of the electron Fermi levels, E_F, so that E_F (semiconductor) = E_F (redox). If, for example, the redox Fermi level before contact is lower than the Fermi level of an n-type semiconductor, a depletion layer will be formed as electrons are extracted by the redox system until equilibration of the Fermi levels is achieved, and the bands will be bent upwards at the interface. For a p-type semiconductor sample, a depletion layer is formed when it is brought into contact with a redox system that has a higher Fermi energy. In this case the bands are bent downwards at the interface. The formation of semiconductor–electrolyte junctions by choosing suitable redox couples is analogous to the formation of metal–semiconductor Schottky junctions by choosing metals with appropriate work functions. This principle is the basis for the design of regenerative photoelectrochemical solar cells, which were widely investigated in the 1980s and achieved remarkably high efficiencies [140]. In practice, adequate stabilization of semiconductor layers for characterization purposes can only be achieved if decomposition reactions are suppressed by choosing electrolytes which capture carriers before they can react with the semiconductor lattice. Usually it is best to choose redox electrolytes that form Schottky barriers since this ensures that minority carriers will be scavenged. Examples include the use of Eu^{3+}/Eu^{2+} couple for p-type materials such as CIS. However, in some cases it may be preferable to use an electrolyte in which the electron transfer process is not only fast but also irreversible. For example Na_2SO_3 is often used with n-type materials like CdS since the SO_3^{2-} ion is an excellent hole scavenger, reacting rapidly and irreversibly to form sulfate.

1.3.3
Photovoltammetry

A rapid assessment of photoactivity and majority carrier type is often required for screening semiconductor layers that have been synthesized for PV applications. This can be achieved (without the need to fabricate an entire device) by using an electrolyte contact and carrying out a cyclic potential sweep while illuminating the electrode with chopped light from a light-emitting diode (LED). The wavelength is usually chosen to lie in the region where the material absorbs strongly, although white (red/green/blue) LEDs are also useful. The sign of the photocurrent can be used to identify the carrier type, and the magnitude gives an indication of the external quantum efficiency (EQE), which is also referred to as the IPCE (incident photon conversion efficiency). The scan also gives information about the behavior of the sample–electrolyte junction in the dark. The presence of pinholes in the film that allow contact between the electrolyte and the substrate can often be inferred from higher dark currents and the appearance of voltammetric

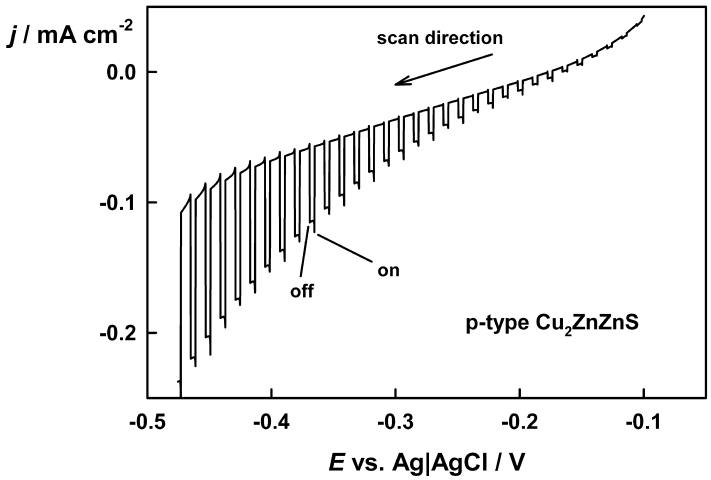

Figure 1.30 Photovoltammogram of a Cu_2ZnSnS_4 layer measured in 0.2 M $Eu(NO_3)_3$ under pulsed illumination from a white LED. The cathodic photoresponse shows that the sample is p-type.

waves associated with oxidation and reduction of the redox couple. Similar effects can be seen if the grain boundaries are quasi-metallic due to impurities or high doping. The transition from depletion to accumulation conditions as a function of applied potential is generally marked by a steep increase in dark current, but this region is best avoided in order to prevent damage to the semiconductor surface.

Photovoltammetry is used routinely in our laboratories to assess new and established materials. Figure 1.30 shows an example of the photovoltammogram recorded for a sample of Cu_2ZnSnS_4 prepared by sulfurization of a stack of three layers of the parent metals [35, 36, 141]. In this case, the electrolyte used contained Eu(III) as an electron scavenger. The cathodic photoresponse confirms that the sample is p-type, and the dark current seen at negative potentials indicates that the film has pinholes that expose the underlying molybdenum film. The photocurrent response to chopped illumination can also be detected using a lock-in amplifier, allowing a more accurate determination of the photocurrent onset potential, which provides an estimate of the flatband potential (the photocurrent for p-type semiconductors onset is usually 200–300 mV more negative than the flatband potential as a consequence of recombination via surface states).

1.3.4
External Quantum Efficiency (EQE) Spectra

The semiconductor–electrolyte junction is essentially an analog of the junction that is formed in a solid-state device such as a solar cell. For this reason, measurements of the EQE as a function of photon energy can be used to obtain information

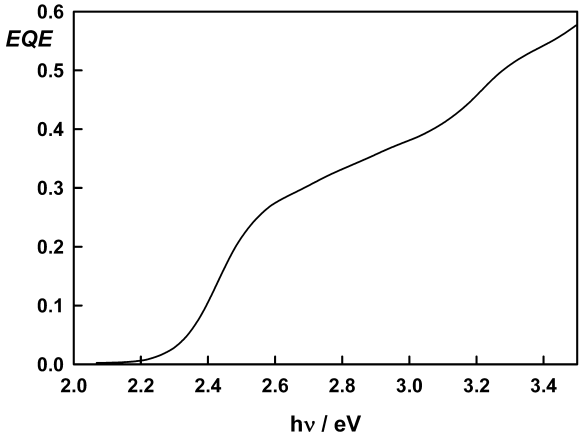

Figure 1.31 EQE spectrum of n-CdS film on FTO glass measured in 0.1 M Na_2SO_3.

about the quality of materials as well as, in some cases, doping densities and minority carrier diffusion lengths.

EQE spectra can be recorded for a range of layer structures that represent different stages in the fabrication of a PV device. In the case of fabrication of CdS/CdTe heterojunction cells by electrodeposition of CdTe onto a thin CdS layer on FTO glass, the EQE response has been used to characterize the CdS films, which are prepared by CBD [142]. Figure 1.31 shows an EQE spectrum measured for an 80 nm CdS film on FTO glass following an annealing in $CdCl_2$ at 415 °C. Analysis of the spectrum using absorbance data obtained by transmission shows that the *internal* quantum efficiency approaches unity over the entire spectral range where the CdS absorbs. As-deposited and air-annealed CdS films have different bandgaps, but they are both photoactive with internal quantum efficiencies approaching unity. Interestingly, the CBD CdS appears to lose its photoactivity entirely when the final structure is annealed to form a CdS/CdTe heterojunction solar cell (this point is discussed in more detail below).

Another interesting example of the application of EQE spectroscopy is its use to follow type conversion in CdS|CdTe heterojunction solar cells fabricated by electrodeposition (see Section 1.2). The method was used originally by Basol on completed solid-state CdS|CdTe cells [143] and later extended by others to characterize partially completed structures using electrolyte contacts [144–147]. The location of the photoactive regions is probed by comparing the EQE spectra for substrate side (SS) and electrolyte side (ES) illumination of the samples as illustrated schematically in Figure 1.32.

As-deposited CdTe films are n-type, so that no heterojunction is formed between the CdTe and the underlying n-type CdS. When the as-deposited CdTe film on CdS is contacted with an electrolyte and is polarized so that a depletion layer forms at the n-CdTe–electrolyte junction, electron–hole pairs generated by illumination are separated, with the holes moving towards the electrolyte interface where they

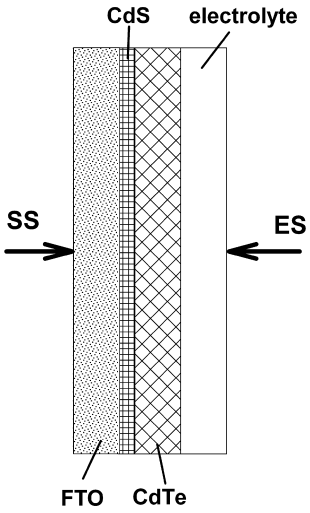

Figure 1.32 Illumination geometry used to study type conversion of CdTe layers on CdS. SS, substrate side illumination; ES, electrolyte side illumination.

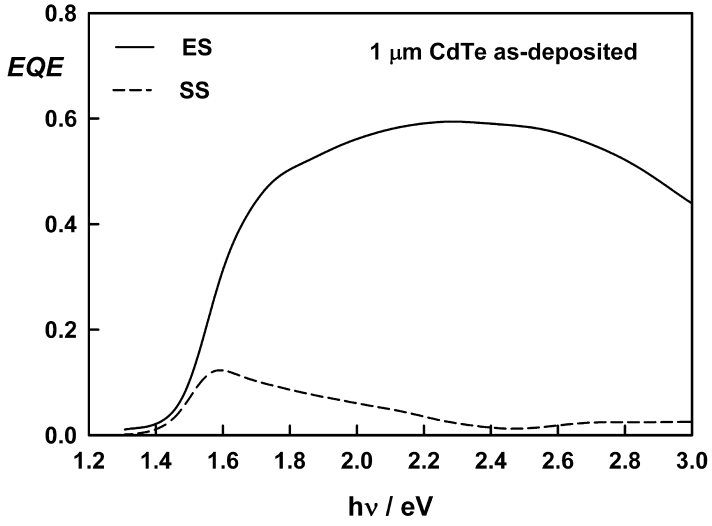

Figure 1.33 EQE spectra for SE and EE illumination of an as-deposited 1 μm CdTe film on CdS/FTO. Comparison of the SE and EE spectra indicates that the CdTe film is n-type.

are scavenged by ions in the electrolyte (0.1 M Na_2SO_3). As Figure 1.33 shows, the EQE spectrum for ES illumination of a 1 μm thick CdTe layer on CdS exhibits an onset at the CdTe bandgap and a fairly flat response at higher photon energies with EQE values of around 0.6. When the illumination is switched to the SS, the

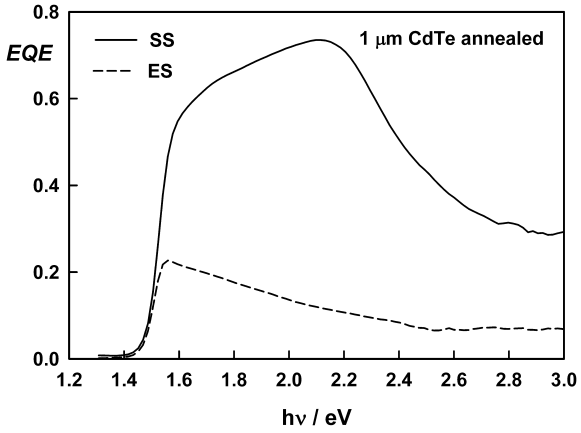

Figure 1.34 SS and ES EQE spectra for CdTe layer on CdS/FTO following type conversion (compare with Figure 1.4).

EQE spectrum shows a maximum near the band edge, but almost no response at higher energies. This indicates that the active junction is indeed located at the CdTe–electrolyte interface, since light can only penetrate through to the CdTe–electrolyte interface from the substrate side when the absorption coefficient of the CdTe is sufficiently low, as is the case near the band edge.

Heating the electrodeposited CdS|CdTe structure in air for 15 minutes at 430 °C converts the CdTe to p-type, forming a heterojunction with the underlying n-CdS. The type conversion process can be followed by measuring the EQE spectra. As Figure 1.34 shows, illumination of the type-converted structure through the glass substrate produces a photocurrent over the entire spectral region above the bandgap of CdTe except for the high-energy region where the CdS absorbs. For SS illumination, the incident light is absorbed close to the n-CdS|p-CdTe junction, and electrons (minority carriers) from the p-CdTe are transferred to the FTO contact via the n-CdS. The "blue" defect seen in the EQE spectrum in the CdS absorption region indicates that the CdS layer is evidently no longer photoactive after the annealing process. This may indicate that the active junction is in fact not at the CdS|CdTe interface but is located inside the CdTe – effectively an n–p homojunction, with no electrical field in the CdS film. The CdS therefore acts as a filter, reducing the response in the blue part of the EQE spectrum. By contrast, after annealing, the EQE spectrum for SE illumination now only exhibits a response near the band edge of the CdTe, since light must be able to penetrate from the electrolyte side through to the internal p–n hetero- or homojunction, which is located close to the substrate contact.

Type conversion has also been followed as a function of annealing time by measuring EQE spectra. Figure 1.35 illustrates how the SS EQE spectra of a 0.5 μm CdTe film on CdS/FTO evolve as the film is annealed. The results show that internal p–n junction is formed after 5 minutes and improves further with

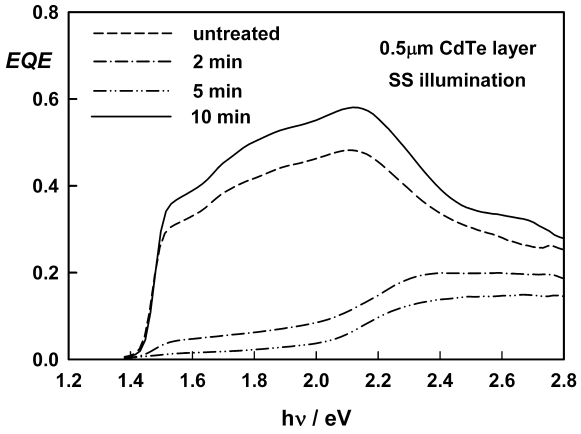

Figure 1.35 EQE spectra for substrate side illumination for CdTe films on CdS/FTO that have been annealed for different times. The spectra show that formation of the p–n junction requires at least 5 minutes annealing time.

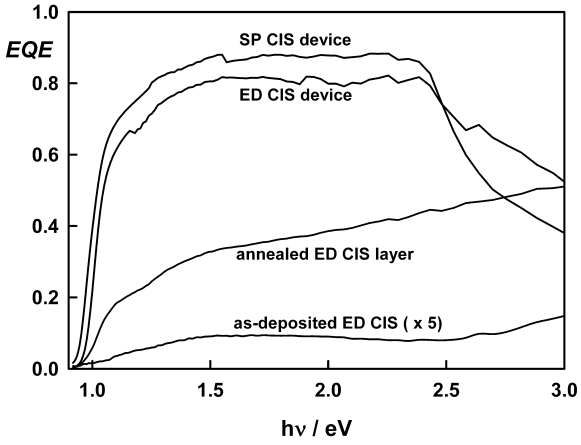

Figure 1.36 EQE spectra of as-deposited and annealed CIS layers compared with the EQE spectra of completed devices based on electrodeposited (ED) and sputtered (SP) CIS layers.

subsequent annealing. Interestingly the spectra also reveal that the CdS layer is photoactive initially but loses its activity when the junction is formed.

Another more recent example of the application of EQE spectra to characterize solar cell absorber layers is shown in Figure 1.36 for different stages in the fabrication of $CuInSe_2$ solar cells. The ED CIS precursor layer was prepared by electrodeposition onto Mo-coated glass, followed by annealing in Se vapor and subsequent etching in KCN to obtain the photoactive material [23] (see Section 1.2). The sputtered CIS device was prepared by magnetron sputtering of a Cu–In

precursor layer followed by annealing in a selenium atmosphere, KCN etching, and deposition of CBD CdS and sputtering of transparent contact layers.

It can be seen that the photoresponse of the as-deposited ED film is very weak – it has been magnified five times in Figure 1.36 to make it visible. The substantial improvement brought about by annealing the ED precursor film in selenium and then etching it in KCN to remove copper selenides is evident from the greatly enhanced EQE response. Interestingly, however, the subsequent fabrication of a device by deposition of CdS and ZnO layers brings about a further improvement, with the finished ED device exhibiting a performance that is almost comparable to that of the sputtered device. It appears that the main reason for this additional improvement is that the CBD of CdS on the CIS film reduces recombination losses substantially. Both devices were fabricated without an antireflection coating, so it can be concluded that the internal quantum efficiency probably approaches unity. The AM 1.5 efficiencies of the finished devices in this study were 6.7% for the ED cell and 8.3% for the sputtered cell. The CdS layer in the finished devices also gives rise to the same "blue" defect in the EQE spectra – the decrease in EQE in the spectral region above 2.4 eV where CdS absorbs the incident light – that is seen in CdTe|CdS devices. The band tailing evident below in the EQE spectra for both ED and sputtered materials probably indicates a high density of sub-bandgap states.

EQE spectra measurements have been used recently as a tool for compositional optimization of Cu_2ZnSnS_4 films prepared by sulfurization of stacked metal layers [35, 36, 141] (see Section 1.2). The spectra shown in Figure 1.37 illustrate the sensitivity of the photoresponse to the Cu/(Zn + Sn) ratio. The highest EQE value (up to 0.4) was obtained for a mean Cu/(Zn + Sn) ratio of 0.86. Recent work in our laboratory has shown that the EQE can be mapped across the surface and correlated with the local composition determined by EDX [36].

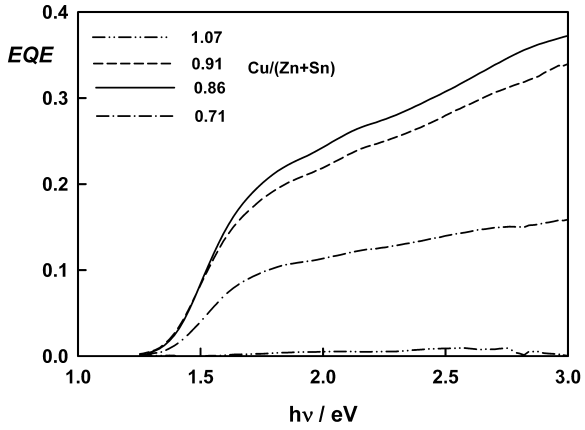

Figure 1.37 EQE spectra of Cu_2ZnSnS_4 layers with different Cu/(Zn + Sn) ratios measured in Eu(III) electrolyte at –0.3 V vs. Ag|AgCl.

EQE spectra can be analyzed to obtain the bandgap of absorber materials. The photocurrent response (j_{photo}) of the semiconductor electrolyte junction is described by the Gärtner equation [148] as

$$EQE = \frac{j_{photo}}{qI_0} = \frac{1 - e^{-\alpha W}}{1 + \alpha L} \tag{1.23}$$

where I_0 is the incident photon flux corrected for reflection losses, α is the absorption coefficient of the absorber at the wavelength of interest, W is the width of the space charge region, and L is the minority carrier diffusion length. For small values of α and L, expansion of the exponential term shows that the EQE becomes linearly proportional to α. For a direct optical transition, the energy dependence of the absorption coefficient is given by

$$\alpha h\nu \propto (h\nu - E_g)^{1/2} \tag{1.24}$$

so that a plot of $(EQE \times h\nu)^2$ vs. photon energy should be linear with an intercept at the bandgap energy E_g. This method is illustrated in Figure 1.38 for $CuInSe_2$ absorber layers prepared by ED and by sputtering (SP) [23]. It can be seen that the two films give slightly different values of E_g. This observation, which appears to be related to the Cu/In ratio in the layers, is discussed in the next section, which deals with the (more precise) determination of bandgaps by electrolyte electroreflectance (EER) spectroscopy.

Doping densities in single-crystal semiconductor samples can usually be determined from capacitance and voltage measurements uing suitable electrolyte contacts. However, in the case thin polycrystalline layers fabricated for PV devices, dark currents arising from cracks and pinholes often make interpretation of impedance data difficult. In this case a different approach based on analysis of the EQE response may be useful. If the minority diffusion length in the sample is sufficiently small to fulfill the condition $\alpha L \ll 1-$as is usually the case for

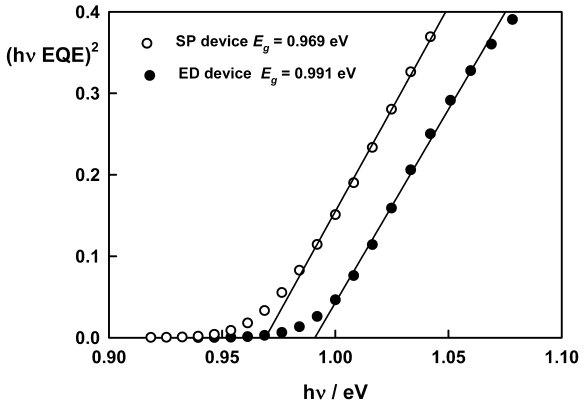

Figure 1.38 Plots used to determine the bandgap of CIS absorber layers from EQE spectra. SP, sputtered film; ED, electrodeposited film.

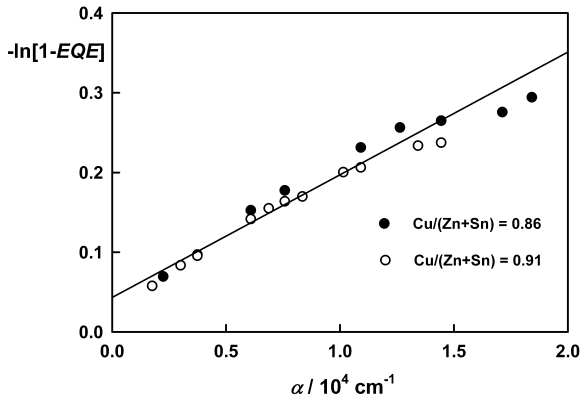

Figure 1.39 Plot used to estimate *W*, the width of the space charge region, and hence the acceptor density for two Cu_2ZnSnS_4 layers with different Cu/(Zn + Sn) ratios.

polycrystalline compound semiconductors – Equation 1.23 can be written in the form

$$-\ln(1-EQE) = \alpha W \tag{1.25}$$

It follows that a plot of –ln(1 – EQE) vs. α should be a linear with a slope equal to the width of the space charge region, *W*, which is given for a p-type semiconductor by

$$W = \left(\frac{2(E_{fb} - E)\varepsilon_0 \varepsilon_r}{qN_a} \right)^{1/2} \tag{1.26}$$

where $(E - E_{fb})$ is the potential relative to the flatband potential E_{fb}, ε_r is the relative permittivity of the material, and N_a is the acceptor density. Figure 1.39 illustrates the application of this method to estimate the doping density in p-type Cu_2ZnSnS_4 samples. The required α values as a function of photon energy were taken from work by Tanaka *et al.* [149], and the flatband potential was estimated from the photocurrent onset (cf. Figure 1.1). The acceptor density obtained from the plot is $3 \times 10^{16}\,cm^{-3}$, a value similar to those reported in the literature for CZTS films prepared by various routes [149, 150].

1.3.5
Electrolyte Electroreflectance/Absorbance: EER/EEA

The technique of EER (or electrolyte electroabsorbance (EEA) in the case of thin films) is a powerful way of determining bandgaps and also of assessing compositional and structural defects. The method is based on perturbing the optical properties of a semiconductor by application of an electric field [151, 152]. The method involves applying an AC modulation to the applied potential when the sample is the working electrode held in depletion conditions in an electrochemical cell to

generate a field in the space charge region. The synchronous modulation of the reflectance or transmittance of the sample is detected using a lock-in amplifier [5]. The changes in reflectance (or transmittance) of the sample brought about by this perturbation generally give rise to sharp third-derivative structures located at critical points in the joint density of states function. A detailed theoretical treatment is outside the scope of this chapter – the interested reader is referred to reviews by Aspnes [151, 152]. For the present purposes, the most important critical point is located at the bandgap energy.

The dependences of EER and EEA spectra on photon energy, E, are generally fitted to a generalized third-derivative fit function given by Aspnes:

$$\frac{\Delta R}{R} \text{ or } \frac{\Delta T}{T} = \mathrm{Re}[Ce^{i\theta}(E - E_g + i\Gamma)] \tag{1.27}$$

where C, θ and Γ are amplitude, phase, and broadening parameters, respectively, and m is a half-integer value that depends on the type of optical transition.

Fitting EER/EEA spectra not only gives precise values of the bandgap but also provides information about the quality of samples. A large value of the broadening parameter Γ can point towards structural or compositional disorder in the sample. An example of the effects of crystallinity on EEA spectra is shown in Figure 1.40. The broad spectrum measured for the air-annealed CBD CdS film on FTO is consistent with the fact that the film is made up of nanocrystallites with sizes of the order of 10 nm [142]. When the film is recrystallized by heating with $CdCl_2$, the spectrum becomes much sharper and the bandgap moves to higher energies. This is consistent with a color change from orange to yellow. In fact in the example shown, the value of Γ for the recrystallized film is actually smaller than the spectral resolution of the monochromator. The EEA spectra show clearly that the recrystallization produces material of high quality.

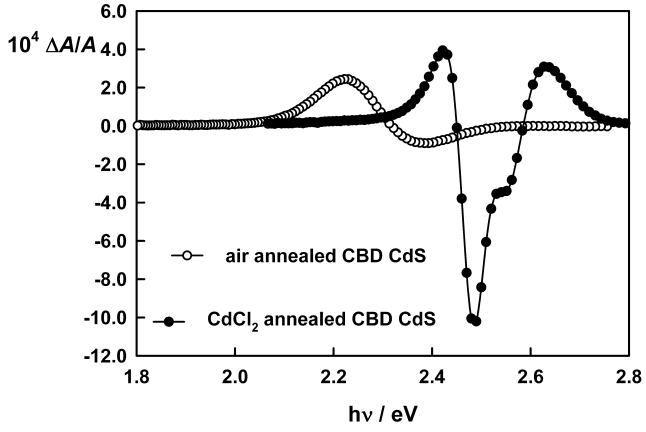

Figure 1.40 Comparison of EEA spectra for air-annealed CdS film on FTO and $CdCl_2$-annealed CdS film showing the effect of recrystallization on the broadening parameter.

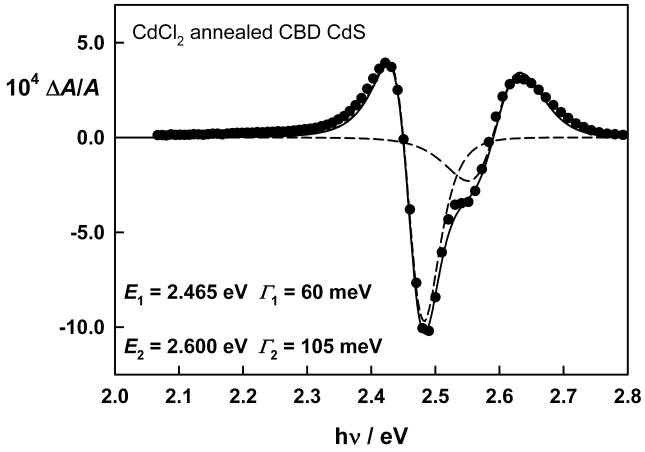

Figure 1.41 Fit of the EEA spectrum of $CdCl_2$-annealed CdS layer on FTO glass to two transitions with the bandgap and broadening parameters shown.

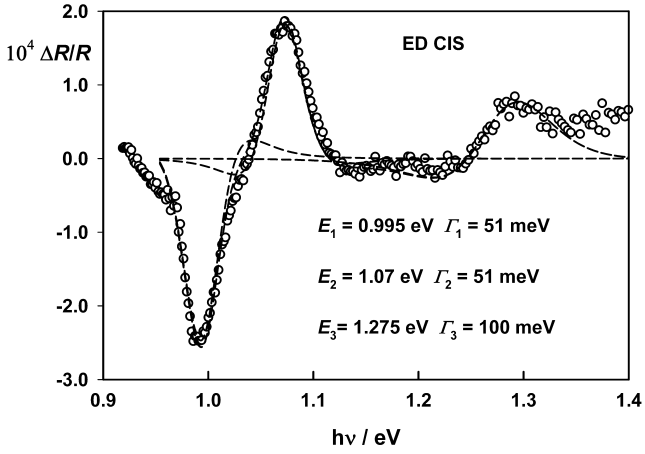

Figure 1.42 Fit of the EER spectrum of an annealed electrodeposited $CuInSe_2$ film.

The fitting of EEA spectra is illustrated in Figure 1.41 for the case of a $CdCl_2$-annealed CdS film. The figure shows that the more complex line shape can be fitted to two transitions at 2.465 and 2.600 eV. Figure 1.42 shows a similar fit of the EER spectrum of a CIS layer, in this case for three optical transitions.

The determination of bandgaps by EER or EEA is illustrated in Figure 1.43, which contrasts the EER spectra measured for ED and SP CIS samples (the spectrum for the sputtered layer is more noisy since the film is rough, scattering a considerable faction of the incident light). The fit for the electrodeposited sample gives a bandgap of 0.99 eV and a broadening parameter of 65 meV. This contrasts with the fit for the sputtered layer, which gives $E_g = 1.00\,\text{eV}$ and $\Gamma = 80\,\text{meV}$.

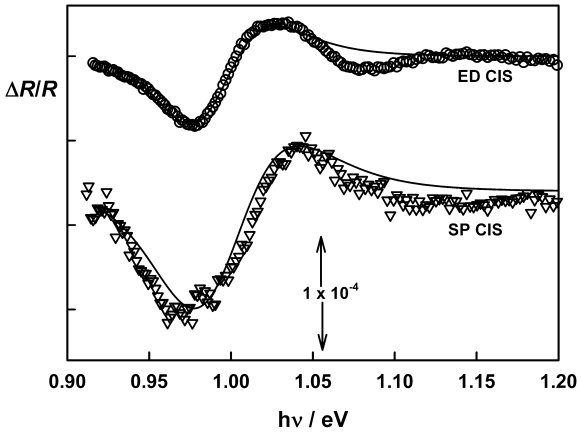

Figure 1.43 EER spectra of electrodeposited (ED) and sputtered (SP) CIS films.

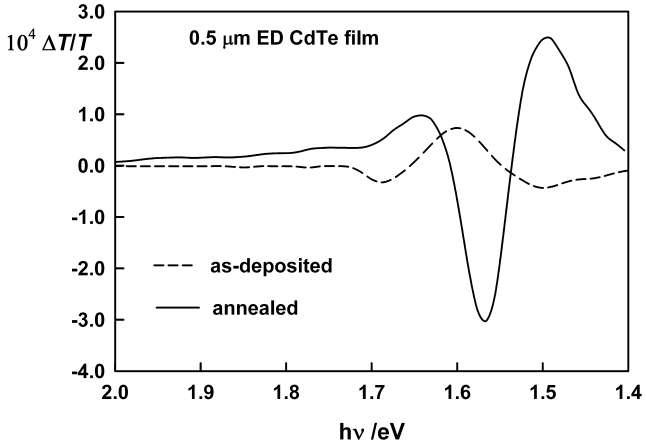

Figure 1.44 EEA spectra of as-deposited and air-annealed CdTe layers on CdS/FTO substrates. The inversion in the peaks is due to conversion of the CdTe from n-type to p-type during annealing.

Shirakata *et al.* [153] have reported EER spectra for single-crystal CIS, and their work indicates that the bandgap depends on the Cu/In ratio in the material, so the difference in E_g values between the ED and SP samples may be significant.

EEA has also been used to follow type conversion in electrodeposited CdTe layers [147]. The change from n-type to p-type is evident in Figure 1.44 as an inversion in the peaks located at the bandgap energy, and a more detailed analysis has shown that the bandgap of the CdTe decreases slightly as a consequence of diffusion of sulfur into the CdTe from the CdS layer to form $CdTe_{1-x}S_x$, where $x = 0.05–0.07$.

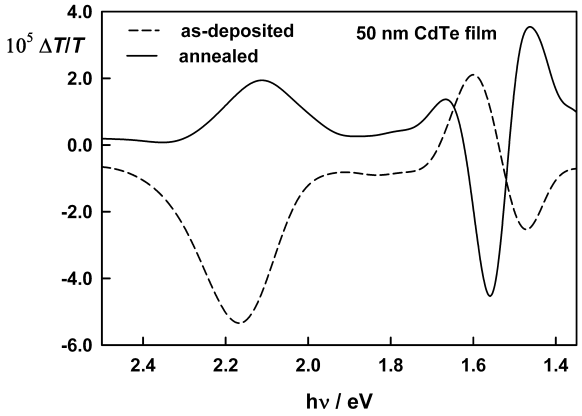

Figure 1.45 EEA spectra of 50 nm CdTe layer on 80 nm CdS film showing effect of air annealing. The structure in the 2.0–2.4 eV range arises from the CdS layer. The lower energy structure is from the CdTe. Note the inversion of both regions brought about by type conversion.

EEA measurements on ultra-thin (50 nm) CdTe layers of electrodeposited CdTe on CdS/FTO show a well-defined response from the CdS layer as well as the CdTe [147], as shown in Figure 1.45. In this case the CdS response is retained after air annealing, indicating that the electric field penetrates into the CdS. This contrasts with the lack of response seen when thicker CdTe films are grown on top of the CdS and air annealed. This suggests that a very thin CdTe film does not supply sufficient Te to diffuse into the CdS during annealing to make it photoinactive.

1.4 Conclusions

This chapter aims to illustrate the considerable potential of electrochemistry as a tool that can be used for the preparation and characterization of materials for thin-film solar cells. Electrochemical methods are not as well established in semiconductor science as they could be. Compared with the industrial importance of electrodeposition of metals for magnetic storage devices and device contacts, the electrodeposition of semiconductors and semiconductor precursors is still underdeveloped. However, the range of relatively sophisticated experimental techniques available to the electrochemist provides a sound basis for further progress. The authors believe that the next few years could see electrochemistry taking a more central position as an enabling technology that will impact on large-scale deployment of photovoltaics as a response to the looming challenges posed by global climate change. The search for new and sustainable materials and fabrication technologies is particularly relevant in this context, and the authors hope that this

chapter will stimulate speculation about further applications of electrochemistry to address real-world problems.

Acknowledgments

The authors would like to thank Florencia Balbastro, Dominik Berg, Johannes Fischer, Masato Kurihara, Jonathan Scragg, and Marc Steichen for their help with the preparation of the manuscript.

References

1 The Economics of Climate Change. Nicholas Stern. Cabinet Office–HM Treasury 2007. ISBN-13: 9780521700801.
2 Beach, J.D. and McCandless, B.E. (2007) *MRS Bull.*, **32**, 225.
3 Feltrin, A. and Freundlich, A. (2008) *Renewable Energy*, **33**, 180.
4 Lincot, D. (2005) *Thin Solid Films*, **487**, 40.
5 Peter, L.M. and Tributsch, H. (2008) In *Nanostructured and Photoeletrochemical Systems for Solar Photon Conversion*. Editors M.D. Archer and A.J. Nozik. Imperial College Press, London.
6 Green, M.A., Emery, K., Hishikawa, Y., and Warta, W. (2009) *Prog. Photovoltaics*, **17**, 320.
7 Bar, M., Repins, I., Contreras, M.A., Weinhardt, L., Noufi, R., and Heske, C. (2009) *Appl. Phys. Lett.*, **95**, 3.
8 Kemell, M., Ritala, M., and Leskela, M. (2005) *Crit. Rev. Solid State Mater. Sci.*, **30**, 1.
9 Katagiri, H., Jimbo, K., Tahara, M., Araki, H., and Oishi, K. (2009) Proceedings of MRS 2009 Spring Meeting, San Francisco.
10 Katagiri, H., Jimbo, K., Yamada, S., Kamimura, T., Maw, W.S., Fukano, T., Ito, T., and Motohiro, T. (2008) *Appl. Phys. Express*, **1**, 041201.
11 Scragg, J.J., Berg, D.M., and Dale, P.J. (2010) *J. Electroanal. Chem.*, **646**, 52.
12 Schorr, S. (2007) *Thin Solid Films*, **515**, 5985.
13 Pauporte, T. and Lincot, D. (2000) *Electrochim. Acta*, **45**, 3345.
14 Miles, R.W., Zoppi, G., and Forbes, I. (2007) *Mater. Today*, **10**, 20.
15 Romeo, A., Terheggen, A., Abou-Ras, D., Batzner, D.L., Haug, F.J., Kalin, M., Rudmann, D., and Tiwari, A.N. (2004) *Prog. Photovoltaics*, **12**, 93.
16 Dale, P.J., Hoenes, K., Scragg, J., and Siebentritt, S. (2009) 34th IEEE Photovoltaic Specialists Conference, vols 1–3, 1956–61, Philadelphia.
17 Sze, S.M. (1985) *Semiconductor Devices Physics and Technology*, John Wiley & Sons, Inc., New York.
18 Wurfel, P. (2005) *Physics of Solar Cells*, Wiley-VCH Verlag GmbH, Weinheim.
19 Pandey, R.K. (1996) *Handbook of Semiconductor Electrodeposition*, 1st edn, CRC.
20 Gregory, B.W. and Stickney, J.L. (1991) *J. Electroanal. Chem.*, **300**, 543.
21 Muthuvel, M. and Stickney, J.L. (2006) *Langmuir*, **22**, 5504.
22 Suggs, D.W., Villegas, I., Gregory, B.W., and Stickney, J.L. (1992) *J. Vac. Sci. Technol. A*, **10**, 886.
23 Dale, P.J., Samantilleke, A.P., Zoppi, G., Forbes, I., and Peter, L.M. (2008) *J. Phys. D*, **41**, 085105.
24 Panicker, M.P.R., Knaster, M., and Kroger, F.A. (1978) *J. Electrochem. Soc.*, **125**, 566.
25 Dennison, S. (1993) *Electrochim. Acta*, **38**, 2395.
26 Kashyout, A.B., Arico, A.S., Monforte, G., Crea, F., Antonucci, V., and Giordano, N. (1995) *Solar Energy Mater. Solar Cells*, **37**, 43.

27 Dale, P.J., Samantilleke, A.P., Shivagan, D.D., and Peter, L.M. (2007) *Thin Solid Films*, **515**, 5751.

28 Bhattacharya, R.N., Fernandez, A., Contreras, M., Keane, J., Tennant, A.L., Ramanathan, K., Tuttle, J.R., Noufi, R., and Hermann, A.M. (1996) *J. Electrochem. Soc.*, **143**, 854.

29 Kroger, F.A. (1978) *J. Electrochem. Soc.*, **125**, 2028.

30 Lincot, D., Guillemoles, J.F., Taunier, S., Guimard, D., Sicx-Kurdi, J., Chaumont, A., Roussel, O., Ramdani, O., Hubert, C., Fauvarque, J.P., Bodereau, N., Parissi, L., Panheleux, P., Fanouillere, P., Naghavi, N., Grand, P.P., Benfarah, M., Mogensen, P., and Kerrec, O. (2004) *Solar Energy*, **77**, 725.

31 Verma, S., Varrin, R.D., Birkmire, R.W., and Russell, T.W.F. (1991) Conference Record of the 22nd IEE Photovoltaic Specialists Conference, Vols 1 and 2.

32 Zank, J., Mehlin, M., and Fritz, H.P. (1996) *Thin Solid Films*, **286**, 259.

33 Kampmann, A., Rechid, J., Raitzig, A., Wulff, S., Mihhailova, R., Thyen, R., and Kalberlah, K. (2003) Proceeding of the MRS Spring Meeting, San Francisco.

34 Voss, T., Schulze, J., Kirbs, A., Palm, J., Probst, V., Jost, S., Hock, R., and Purwins, M. (2007) 22nd European Photovoltaic Solar Energy Conference, 3–7 September 2007, Milan.

35 Scragg, J.J., Dale, P.J., and Peter, L.M. (2008) *Electrochem. Commun.*, **10**, 639.

36 Scragg, J.J., Dale, P.J., and Peter, L.M. (2009) *Thin Solid Films*, **517**, 2481.

37 Scragg, J.J., Dale, P.J., Peter, L.M., Zoppi, G., and Forbes, I. (2008) *Phys. Stat. Sol. (b)*, **245**, 1772.

38 Reference deleted.

39 Araki, H., Kubo, Y., Mikaduki, A., Jimbo, K., Maw, W.S., Katagiri, H., Yamazaki, M., Oishi, K., and Takeuchi, A. (2009) *Solar Energy Mater. Solar Cells*, **93**, 996.

40 Reference deleted.

41 Guillen, C. and Herrero, J. (1996) *J. Electrochem. Soc.*, **143**, 493–8.

42 Fischer, J., Dale, P.J., and Siebentritt, S. (2009) 216th Electrochemical Society, Vienna.

43 Basol, B.M. and Tseng, E.S.F. (1983) *J. Electrochem. Soc.*, **130**, C243.

44 Calixto, M.E., Dobson, K.D., McCandless, B.E., and Birkmire, R.W. (2005) Conference Record of the 31st IEEE Photovoltaic Specialists Conference, p. 378.

45 Miller, B., Menezes, S., and Heller, A. (1978) *J. Electroanal. Chem.*, **94**, 85.

46 Menezes, S., Miller, B., and Heller, A. (1979) *J. Electrochem. Soc.*, **126**, C376.

47 Peter, L.M. (1979) *J. Electroanal. Chem.*, **98**, 49.

48 Miller, B. and Heller, A. (1976) *Nature*, **262**, 680.

49 Peter, L.M. (1978) *Electrochim. Acta*, **23**, 1073.

50 Peter, L.M. (1978) *Electrochim. Acta*, **23**, 165.

51 Riveros, G., Guillemoles, J.F., Lincot, D., Meier, H.G., Froment, M., Bernard, M.C., and Cortes, R. (2002) *Adv. Mater.*, **14**, 1286.

52 Baranski, A.S., Bennett, M., and Fawcett, W.R. (1983) *J. Electrochem. Soc.*, **130**, C110.

53 Fatas, E., Duo, R., Herrasti, P., Arjona, F., and Garciacamarero, E. (1984) *J. Electrochem. Soc.*, **131**, 2243.

54 Freyland, W., Zell, C.A., Abedin, S.Z.E., and Endres, F. (2003) *Electrochim. Acta*, **48**, 3053.

55 Gregory, B.W., Suggs, D.W., and Stickney, J.L. (1991) *J. Electrochem. Soc.*, **138**, 1279.

56 Basol, B.M., Ou, S.S., and Stafsudd, O.M. (1984) *J. Appl. Phys.*, **58**, 3809.

57 Rajeshwar, K., and Bhattacharya, R.N. (1984) *J. Electrochem. Soc.*, **131**, C314.

58 Rajeshwar, K., Bhattacharya, R.N., and Ho, S.I. (1984) *J. Electrochem. Soc.*, **131**, C313.

59 Bhattacharya, R.N. and Rajeshwar, K. (1985) *J. Appl. Phys.*, **58**, 3590.

60 Bhattacharya, R.N., Rajeshwar, K., and Noufi, R.N. (1985) *J. Electrochem. Soc.*, **132**, 732.

61 Turner, A.K., Woodcock, J.M., Ozsan, M.E., Cunningham, D.W., Johnson, D.R., Marshall, R.J., Mason, N.B., Oktik, S., Patterson, M.H., Ransome,

S.J., Roberts, S., Sadeghi, M., Sherborne, J.M., Sivapathasundaram, D., and Walls, I.A. (1994) *Solar Energy Mater. Solar Cells*, **35**, 263.
62 Cunningham, D., Rubcich, M., and Skinner, D. (2002) *Prog. Photovoltaics*, **10**, 159.
63 Saraby-Reintjes, A., Peter, L.M., Ozsan, M.E., Dennison, S., and Webster, S. (1993) *J. Electrochem. Soc.*, **140**, 2880.
64 Mori, E. and Rajeshwar, K. (1989) *J. Electroanal. Chem.*, **258**, 415.
65 Danaher, W.J. and Lyons, L.E. (1984) *Aust. J. Chem.*, **37**, 689.
66 Engelken, R.D. and Vandoren, T.P. (1985) *J. Electrochem. Soc.*, **132**, 2904.
67 Sella, C., Boncorps, P., and Vedel, J. (1986) *J. Electrochem. Soc.*, **133**, 2043.
68 Colletti, L.P. and Stickney, J.L. (1998) *J. Electrochem. Soc.*, **145**, 3594.
69 Stickney, J.L. (1999) *Electroanal. Chem.*, **21**, 75.
70 Cowache, P., Lincot, D., and Vedel, J. (1989) *J. Electrochem. Soc.*, **136**, 1646.
71 Lincot, D., Kampmann, A., Mokili, B., Vedel, J., Cortes, R., and Froment, M. (1995) *Appl. Phys. Lett.*, **67**, 2355.
72 Wagner, S., Shay, J.L., Migliorato, P., and Kasper, H.M. (1974) *Appl. Phys. Lett.*, **25**, 434.
73 Bhattacharya, R.N. (1983) *J. Electrochem. Soc.*, **130**, 2040.
74 Hodes, G., Engelhard, T., Cahen, D., Kazmerski, L.L., and Herrington, C.R. (1985) *Thin Solid Films*, **128**, 93.
75 Kapur, V.K., Basol, B.M., and Tseng, E.S. (1987) *Solar Cells*, **21**, 65–72.
76 Kessler, J., Sicx-Kurdi, J., Naghavi, N., Guillemoles, J.F., Lincot, D., Kerrec, O., Lamirand, M., Legras, L., and Mogensen, P. (2005) 20th European Photovoltaic Solar Energy Conference, 6–10 June 2005, Barcelona.
77 Guillemoles, J.F., Lusson, A., Cowache, P., Massaccesi, S., Vedel, J. and Lincot, D. (1994) *Adv. Mater.*, **6**, 376–9.
78 Chassaing, E., Grand, P.-P., Etcheberry, A., and Lincot, D. (2009) *ECS Trans.*, **19**, 149.
79 Calixto, M.E., Sebastian, P.J., Bhattacharya, R.N., and Noufi, R. (1999) *Solar Energy Mater. Solar Cells*, **59**, 75.
80 Probst, V., Palm, J., Visbeck, S., Niesen, T., Tolle, R., Lerchenberger, A., Wendl, M., Vogt, H., Calwer, H., Stetter, W., and Karg, F. (2006) *Solar Energy Mater. Solar Cells*, **90**, 3115.
81 Palm, J., Probst, V., Brummer, A., Stetter, W., Tolle, R., Niesen, T.P., Visbeck, S., Hernandez, O., Wendl, M., Vogt, H., Calwer, H., Freienstein, B., and Karg, F. (2003) *Thin Solid Films*, **431**, 514.
82 Pourbaix, M. (1974) *Atlas of Electrochemical Equilibria in Aqueous Solutions*, NACE International Cebelcor.
83 Penndorf, J., Winkler, M., Tober, O., Roser, D., and Jacobs, K. (1998) *Solar Energy Mater. Solar Cells*, **53**, 285.
84 Barbosa, L.L., de Almeida, M.R.H., Carlos, R.M., Yonashiro, M., Oliveira, G.M., and Carlos, I.A. (2005) *Surf. Coat. Technol.*, **192**, 145.
85 Walsh, F.C. and Gabe, D.R. (1979) *Surface Technology*, **8**, 87–99.
86 Kampmann, A., Rechid, J., Wulff, S., Mihhailova, R., Thyen, R., and Lossin, A. (2004) 19th European Photovoltaic Solar Energy Conference, Paris, p. 1806.
87 Jost, S., Hergert, F., Hock, R., Schulze, J., Kirbs, A., Voss, T., and Purwins, M. (2007) *Solar Energy Mater. Solar Cells*, **91**, 1669.
88 Jost, S., Hergert, F., Hock, R., Schulze, J., Kirbs, A., Voss, T., Purwins, M., and Schmid, M. (2007) *Solar Energy Mater. Solar Cells*, **91**, 636.
89 Jost, S., Hergert, F., Hock, R., Voss, T., Schulze, J., Kirbs, A., Purwins, M., Probst, V., and Palm, J. (2007) *Thin-Film Compound Semiconductor Photovoltaics–2007*, ed T. Gessert, *et al.* (Warrendale: Materials Research Society) pp 175–80.
90 Jost, S., Schurr, R., Hergert, F., Hock, R., Schulze, J., Kirbs, A., Voss, T., Purwins, M., Palm, J., and Mys, I. (2008) *Solar Energy Mater. Solar Cells*, **92**, 410.
91 Siemer, K., Klaer, J., Luck, I., Bruns, J., Klenk, R., and Braunig, D. (2001) *Solar Energy Mater. Solar Cells*, **67**, 159.
92 Friedfeld, R., Raffaelle, R.P., and Mantovani, J.G. (1999) *Solar Energy Mater. Solar Cells*, **58**, 375.
93 Kois, J., Ganchev, M., Kaelin, M., Bereznev, S., Tzvetkova, E., Volobujeva,

O., Stratieva, N., and Tiwari, A.N. (2008) *Thin Solid Films*, **516**, 5948.
94 Massaccesi, S., Sanchez, S., and Vedel, J. (1993) *J. Electrochem. Soc.*, **140**, 2540–6.
95 Lippkow, D. and Strehblow, H.H. (1998) *Electrochim. Acta*, **43**, 2131.
96 Massaccesi, S., Sanchez, S., and Vedel, J. (1996) *J. Electroanal. Chem.*, **412**, 95.
97 Aksu, S., Wang, J.X., and Basol, B.M. (2009) *Electrochem. Solid State Lett.*, **12**, D33.
98 Kim, S., Kim, W.K., Kaczynski, R.M., Acher, R.D., Yoon, S., Anderson, T.J., Crisalle, O.D., Payzant, E.A., and Li, S.S. (2005) *J. Vac. Sci. Technol. A*, **23**, 310.
99 Kim, W.K., Kim, S., Payzant, E.A., Speakman, S.A., Yoon, S., Kaczynski, R.M., Acher, R.D., Anderson, T.J., Crisalle, O.D., Li, S.S., and Craciun, V. (2005) *J. Phys. Chem. Solids*, **66**, 1915.
100 Cahen, D. and Noufi, R. (1992) *J. Phys. Chem. Solids*, **53**, 991.
101 Hermann, A.M., Mansour, M., Badri, V., Pinkhasov, B., Gonzales, C., Fickett, F., Calixto, M.E., Sebastian, P.J., Marshall, C.H., and Gillespie, T.J. (2000) *Thin Solid Films*, **361**, 74.
102 Hermann, A.M., Westfall, R., and Wind, R. (1998) *Solar Energy Mater. Solar Cells*, **52**, 355.
103 Thouin, L., Sanchez, S., and Vedel, J. (1993) *Electrochim. Acta*, **38**, 2387.
104 Mishra, K.K. and Rajeshwar, K. (1989) *J. Electroanal. Chem.*, **271**, 279.
105 Thouin, L., Massaccesi, S., Sanchez, S., and Vedel, J. (1994) *J. Electroanal. Chem.*, **374**, 81.
106 Thouin, L. and Vedel, J. (1995) *J. Electrochem. Soc.*, **142**, 2996.
107 Chassaing, E., Grand, P.-P., Saucedo, E., Etcheberry, A., and Lincot, D. (2009) *ECS Trans.*, **19**, 189.
108 Chassaing, E., Guillemoles, J.-F., and Lincot, D. (2009) *ECS Trans.*, **19**, 1.
109 Chassaing, E., Ramdani, O., Grand, P.P., Guillemoles, J.F., and Lincot, D. (2008) *Phys. Stat. Sol. (c)*, **5**, 3445.
110 Calixto, M.E., Dobson, K.D., McCandless, B.E., and Birkmire, R.W. (2006) *J. Electrochem. Soc.*, **153**, G521.
111 Bhattacharya, R.N., Batchelor, W., Granata, J.E., Hasoon, F., Wiesner, H., Ramanathan, K., Keane, J., and Noufi, R.N. (1998) *Solar Energy Mater. Solar Cells*, **55**, 83.
112 Kemell, M., Ritala, M., and Leskela, M. (2001) *J. Mater. Chem.*, **11**, 668.
113 Kemell, M., Saloniemi, H., Ritala, M., and Leskela, M. (2001) *J. Electrochem. Soc.*, **148**, C110.
114 Nomura, S., Nishiyama, K., Tanaka, K., Sakakibara, M., Ohtsubo, M., Furutani, N., and Endo, S. (1998) *Jpn. J. Appl. Phys. Part 1*, **37**, 3232.
115 Ito, K. and Nakazawa, T. (1988) *Jpn. J. Appl. Phys. Part 1*, **27**, 2094.
116 Dale, P.J., Hoenes, K., Scragg, J., and Siebentritt, S. (2009) 34th IEEE Photovoltaic Specialists Conference, Vols 1–3, (New York: IEEE) pp 1956–61.
117 Katagiri, H. (2005) *Thin Solid Films*, **480–481**, 426.
118 Schubert, B., Marsen, B., Cinque, S., Unold, T., Klenk, R., Schorr, S., and Schock, H.W. Progress in Photovoltaics: Research and Applications DOI: 10.1002/pip.976
119 Araki, H., Kubo, Y., Mikaduki, A., Jimbo, K., Maw, W.S., Katagiri, H., Yamazaki, M., Oishi, K., and Takeuchi, A. (2007) 17th International Photovoltaic Science and Engineering Conference, Fukuoka, p. 996.
120 Araki, H., Kubo, Y., Jimbo, K., Maw, W.S., Katagiri, H., Yamazaki, M., Oishi, K., and Takeuchi, A. (2009) *Physica Status Solidi (C) Current Topics in Solid State Physics*, **6**, 1266–8.
121 Ennaoui, A., Lux-Steiner, M., Weber, A., Abou-Ras, D., Kötschau, I., Schock, H.W., Schurr, R., Hölzing, A., Jost, S., Hock, R., Voß, T., Schulze, J., and Kirbs, A. (2009) *Thin Solid Films*, **517**, 2511.
122 Kurihara, M., Berg, D., Fischer, J., Siebentritt, S., and Dale, P.J. (2009) *Phys. Stat. Sol. (c)*, **6**, 1241.
123 Broggi, R.L., Oliveira, G.M.D., Barbosa, L.L., Pallone, E., and Carlos, I.A. (2006) *J. Appl. Electrochem.*, **36**, 403.
124 Araki, H., Mikaduki, A., Kubo, Y., Sato, T., Jimbo, K., Maw, W.S., Katagiri, H., Yamazaki, M., Oishi, K., and Takeuchi, A. (2008) *Thin Solid Films*, **517**, 1457.

125 Hergert, F. and Hock, R. (2007) *Thin Solid Films*, **515**, 5953.

126 Schurr, R., Holzing, A., Jost, S., Hock, R., Voss, T., Schulze, J., Kirbs, A., Ennaoui, A., Lux-Steiner, M., Weber, A., Kotschau, I., and Schock, H.W. (2008) Symposium on Thin Film Chalcogenide Photovoltaic Materials held at the EMRS 2008 Spring Conference, Strasbourg, p. 2465.

127 Chou, C.Y. and Chen, S.W. (2006) *Acta Mater.*, **54**, 2393.

128 Olekseyuk, I.D., Dudchak, I.V., and Piskach, L.V. (2004) *J. Alloys Compd*, **368**, 135.

129 Abedin, S.Z.E. and Endres, F. (2006) *ChemPhysChem*, **7**, 58.

130 Shivagan, D.D., Dale, P.J., Samantilleke, A.P., and Peter, L.M. (2007) *Thin Solid Films*, **515**, 5899.

131 Abedin, S.Z.E., Saad, A.Y., Farag, H.K., Borisenko, N., Liu, Q.X., and Endres, F. (2007) *Electrochim. Acta*, **52**, 2746.

132 Gasparotto, L.H.S., Borisenko, N., Hofft, O., Al-Salman, R., Maus-Friedrichs, W., Bocchi, N., Abedin, S.Z.E., and Endres, F. (2009) *Electrochim. Acta*, **55**, 218.

133 Yang, M.H., Yang, M.C., and Sun, I.W. (2003) *J. Electrochem. Soc.*, **150**, C544.

134 Hsiu, S.I. and Sun, I.W. (2004) *J. Appl. Electrochem.*, **34**, 1057.

135 Pleskov, Y.V. and Gurevich, Y.Y. (1985) *Semiconductor Photoelectrochemistry*, Consultants Bureau, New York.

136 Sato, N. (1998) *Electrochemistry at Metal and Semiconductor Electrodes*, Elsevier, Amsterdam.

137 Memming, R. (2001) *Semiconductor Electrochemistry*, Wiley-VCH Verlag GmbH, Weinheim.

138 Licht, S., Bard, A.J., and Stratmann, M. (2002) *Encyclopedia of Electrochemistry, Volume 6: Semiconductor Electrodes and Photoelectrochemistry*, Wiley-VCH Verlag GmbH, Weinheim.

139 Schroder, D.K. (1998) *Semiconductor Material and Device Characterization*, 2nd edn, John Wiley & Sons, Inc., New York.

140 Pleskov, Y. (1990) *Solar Energy Conversion. A Photoelectrochemical Approach*, Springer, Berlin.

141 Scragg, J.J., Dale, P.J., Peter, L.M., Zoppi, G., and Forbes, I. (2008) *Phys. Stat. Sol. (b)*, **245**, 1772.

142 Ozsan, M.E., Johnson, D.R., Sadeghi, M., Sivapathasundaram, D., Goodlet, G., Furlong, M.J., Peter, L.M., and Shingleton, A.A. (1996) *J. Mater. Sci. Mater. Electron.*, **7**, 119.

143 Basol, B.M. (1984) *J. Appl. Phys.*, **55**, 601.

144 Kampmann, A., Cowache, P., Vedel, J., and Lincot, D. (1995) *J. Electroanal. Chem.*, **387**, 53.

145 Duffy, N.W., Lane, D., Ozsan, M.E., Peter, L.M., Rogers, K.D., and Wang, R.L. (2000) *Thin Solid Films*, **36**, 314.

146 Duffy, N.W., Peter, L.M., Wang, R.L., Lane, D.W., and Rogers, K.D. (2000) *Electrochim. Acta*, **45**, 3355.

147 Duffy, N.W., Peter, L.M., and Wang, R.L. (2002) *J. Electroanal. Chem.*, **532**, 207.

148 Gartner, W.W. (1959) *Phys. Rev.*, **116**, 84.

149 Tanaka, T., Nagatomo, T., Kawasaki, D., Nishio, M., Guo, Q.X., Wakahara, A., Yoshida, A., and Ogawa, H. (2005) *J. Phys. Chem. Solids*, **66**, 1978.

150 Kobayashi, T., Jimbo, K., Tsuchida, K., Shinoda, S., Oyanagi, T., and Katagiri, H. (2005) *Jpn. J. Appl. Phys.*, **44**, 783.

151 Aspnes, D.E. (1973) *Surf. Sci.*, **37**, 418.

152 Aspnes, D.E. (1980) *Handbook on Semiconductors*, vol. 2 (ed. M. Balkanski), North Holland, New York, p. 109.

153 Shirakata, S., Chichibu, S., Isomura, S., and Nakanishi, K. (1997) *Jpn. J. Appl. Phys. Part 2*, **36**, L543.